inorganics

MDPI

Article

Naphthyl-Containing Organophosphonate Derivatives of Keggin-Type Polyoxotungstates

Nerea Andino [1], Beñat Artetxe [1,2,*], Santiago Reinoso [1,*], Pablo Vitoria [1], Leire San Felices [3], Jose I. Martínez [4], Fernando López Arbeloa [2,5] and Juan M. Gutiérrez-Zorrilla [1,2]

1 Departamento de Química Inorgánica, Facultad de Ciencia y Tecnología, Universidad del País Vasco UPV/EHU, Bilbao 48080, Spain; nandino001@ikasle.ehu.es (N.A.); pablo.vitoria@ehu.es (P.V.); juanma.zorrilla@ehu.es (J.M.G.-Z.)

2 BCMaterials, Parque Científico y Tecnológico de Bizkaia, Derio 48160, Spain; fernando.lopezarbeloa@ehu.es

3 Servicios Generales de Investigación SGIker, Universidad del País Vasco UPV/EHU, Bilbao 48080, Spain; leire.sanfelices@ehu.es

4 Departamento de Química Orgánica II, Facultad de Ciencia y Tecnología, Universidad del País Vasco UPV/EHU, Bilbao 48080, Spain; joseignacio.martinezf@ehu.es

5 Departamento de Química Física, Facultad de Ciencia y Tecnología, Universidad del País Vasco UPV/EHU, Bilbao 48080, Spain

* Correspondence: benat.artetxe@ehu.es (B.A.); santiago.reinoso@ehu.es (S.R.); Tel.: +34-94-601-5522 (B.A. & S.R.); Fax: +34-94-601-3500 (B.A. & S.R.)

Academic Editors: Greta Ricarda Patzke and Lee J. Higham
Received: 31 March 2016; Accepted: 3 May 2016; Published: 12 May 2016

Abstract: New organophosphonate derivatives of monovacant Keggin-type polyoxotungstates that contain naphthyl groups have been synthesized and characterized in both solid state and solution. Single-crystal structural analysis shows that two phosphonate groups occupy the vacant position of the lacunary cluster unit in the isostructural compounds $[N(C_4H_9)_4]_3[H(POC_{11}H_9)_2(\alpha\text{-}HBW_{11}O_{39})]$ (**TBA-1**) and $[N(C_4H_9)_4]_3[H(POC_{11}H_9)_2(\alpha\text{-}SiW_{11}O_{39})]$ (**TBA-2**). Liquid-solution UV–Vis transmittance and solid-state diffuse reflectance spectroscopy studies reveal the presence of a new absorption band in the visible region, the charge transfer character of which has been further confirmed by time-dependent density functional theory (TD-DFT) calculations. The latter evidence that the charge transfer process is dominated by transitions from the highest occupied molecular orbital (HOMO), localized in the aromatic ring of the organic group, to the lowest unoccupied molecular orbital (LUMO), localized in the Keggin anion. Photoluminescence studies show that the fluorescent properties of the 1-naphthylmethylphosphonate group are quenched upon its incorporation into the inorganic oxo-tungstate skeleton. The solution stability of the hybrid clusters has been evaluated by a combination of ^{1}H-, ^{13}C- and ^{31}P-Nuclear Magnetic Resonance spectroscopy and Electrospray Ionization-Mass Spectrometry. The hybrid polyanion $[H(POC_{11}H_9)_2(\alpha\text{-}HBW_{11}O_{39})]^{3-}$ (**1**) herein constitutes the first structurally characterized organo-p-block containing borotungstate, and hence it confirms that this strategy for the organic functionalization of polyoxometalate clusters can be applied to new platforms belonging to the family of group-13 heteropolyoxotungstates.

Keywords: polyoxometalates; organophosphonates; charge transfer; fluorescence; solution stability

1. Introduction

The organic derivatization of polyoxometalates (POMs) represents one of the most relevant topics within the chemistry of this well-known family of anionic metal-oxo clusters with applications in current fields of interest such as catalysis, medicine and materials science [1–5]. The resulting organic–inorganic hybrids avoid the processing drawbacks that unmodified POMs can display for

being incorporated into functional architectures or devices [6–8]. The covalent attachment of organic molecules to POM skeletons can confer tuned properties on the resulting hybrid species and can also allow for the immobilization of the clusters on diverse surfaces or matrixes. Nevertheless, highly elaborate functionalities for applications in, e.g., optics, molecular electronics or sensing often require the postfunctionalization of preformed hybrid POM platforms via multistep synthetic work [9].

Three main synthetic methods have been developed to prepare well-defined, solution-stable molecular hybrid POMs [10]. These include strategies involving the replacement of shell O atoms with O- or N-donor ligands as exemplified by tris(alkoxo)-capped Anderson–Evans clusters [11], hexavanadates [12] or $[H_4P_2V_3W_{15}O_{62}]^{5-}$ anions [13], as well as by organoimido/diazenido derivatives of Lindqvist-type molybdates [14]. Another approach is based on the reaction between 3d- and/or 4f-metal substituted POMs with exposed centers toward multidentante organic ligands [15–18]. However, the most explored route consists in combining lacunary polyoxotungstates with p-block organoderivatives. The nucleophilic character of the oxygen atoms delimiting the lacunae is significantly increased compared with those of the plenary anion, and this greatly favors the reaction with electrophilic groups. The use of organotin entities has resulted in some interesting compounds [19–21] and a few examples of organogermyl, -arsenyl and -stibyl functionalized POMs can also be found in the literature [22,23]. Nevertheless, organosilyl and -phosphoryl groups constitute the derivatizing agents that have attracted the greatest interest since the first report by Knoth in the early 1980s [24].

In the case of organosilyl derivatives, a large variety of functionalities have been incorporated into monolacunary Keggin or Wells–Dawson anions containing up to two organogroups or one dimeric μ-oxo-bridged $(RSi)_2O$ unit per vacant site [25,26]. In regard to di- and trilacunary anions, two to four organosilyl entities have been selectively anchored to the POM vacant sites [27,28]. The functionalization of mono-, di- and trilacunary Keggin-type phospho- or silicotungstates with organophosphonate moieties has been thoroughly explored as well [29–31]. Some reports on the reactivity of Wells–Dawson $[P_2W_{17}O_{61}]^{10-}$ and Keggin-type $[XW_{11}O_{39}]^{n-}$ (X = B, Ga, Ge) monovacant frameworks can be found in the literature, but they do not include any X-ray crystal structure analysis [32–34]. The immobilization of such type of hybrid POM platforms in silica matrixes [35], metallic [36,37] or polymeric [38] nanoparticles, and silicon or metallic surfaces has resulted in advanced functional materials targeting the heterogenization of homogeneous catalysts [39], molecular memories [40] and selective biomolecule-adhesion properties [41].

In order to incorporate custom-designed organic moieties to the clusters, two strategies are usually followed. The first approach consists in preparing the desired p-block organo-group, followed by its reaction with lacunary POMs. In the second method, the p-block organoderivative with a reactive pendant group is first inserted in the vacant site of the cluster and the resulting hybrid POM species is then used as platform for further postfunctionalization. Following these two synthetic routes and making use of click chemistry or Pd catalyzed coupling reactions, photoactive electron transfer complexes that mimic the bio-inspired artificial photosynthesis have been prepared among others [42–45]. Magnetically and catalytically active d-metal centers have also been included in the structure by using organic functionalities suitable for metal coordination [46]. Alternatively, oxophilic 3d- or 4f-metals have been incorporated by taking advantage of the free and accessible O atoms in the phosphonate groups of Keggin-type POM derivatives [47,48]. Organophosphonate-functionalized POM species have shown interesting catalytic properties for oxidation reactions by themselves [49], and furthermore, compounds bearing coordinated metal centers represent original molecular models for isolated single-site catalytic species dispersed onto matrixes like silica [50].

Herein we report the synthesis and full characterization in both the solid state and liquid solution of 1-naphthylmethylphosphonate-containing derivatives of monovacant Keggin anions, namely $[N(C_4H_9)_4]_3[H(POC_{11}H_9)_2(HBW_{11}O_{39})]$ (**TBA-1**) and $[N(C_4H_9)_4]_3[H(POC_{11}H_9)_2(\alpha\text{-}SiW_{11}O_{39})]$ (**TBA-2**). These hybrid POM platforms have been prepared with the aim of being functionalized with 3d- or 4f-metal centers as models for supported site-isolated catalysts with an aromatic environment.

The aromatic 1-naphthylmethylphosphonate subunit should not only confer photoactive properties on the system, but could also enhance the selectivity of the catalytic process by interacting with the substrate and providing steric hindrance. We selected the $[HBW_{11}O_{39}]^{8-}$ anion for our studies to determine whether borotungstates could be organically derivatized following this route in spite of its peculiar reactivity when compared with analogues that contain heteroatoms from groups 14 and 15, and we employed the isomorphic and topologically equivalent $[SiW_{11}O_{39}]^{8-}$ as pattern in the reaction with 1-naphthylmethylphosphonic acid.

2. Results and Discussion

2.1. Synthesis, Infrared Spectroscopy and Thermal Analyses

Organic functionalization of Keggin-type anions with organophosphonate groups was carried out using the well-established method for the incorporation of organosilyl and -phosphoryl moieties into lacunary POM anions developed by Mayer and Thouvenot [30]. Stoichiometric reactions of the monolacunary Keggin-type anions $[H_nXW_{11}O_{39}]^{8-}$ (X = B, n = 1; X = Si, n = 0) and 1-naphthylmethylphosphonic acid in acetonitrile were carried out with tetrabutylammonium (TBA) bromide as phase transfer agent to dissolve the POM cluster in the organic media. After an overnight reflux and filtering KBr and traces of unreacted POM precursor off, the crude products were obtained upon solvent removal under vacuum. According to ^{31}P-NMR experiments, these crude products were not pure as multiple signals were observed in the spectra. Recrystallization in acetonitrile allowed us not only to obtain single crystals suitable for X-ray diffraction studies, but also to isolate the title compounds as pure, homogeneous phases. All the further characterization was performed on these pure crystalline batches.

The original synthesis was carried out employing the $[HBW_{11}O_{39}]^{8-}$ anion as POM precursor to evaluate whether lacunary heteropolytunsgtates with heteroatoms of the group 13 can act as inorganic platforms for their derivatization with p-block organo-groups. This question is yet to be experimentally confirmed as straightforward analogies with other monovacant Keggin-type species are usually unfeasible due to the peculiar behavior of borotungstates in aqueous solution when compared with isoelectronic species like $[XW_{11}O_{39}]^{8-}$ (X = Si, Ge). For example, the reaction of tungstate ions with $[HBW_{11}O_{39}]^{8-}$ does not directly lead to the plenary α-$[BW_{12}O_{40}]^{5-}$ Keggin ion. Instead, one ditungstate fragment places over the vacant site to lead to the $[BW_{13}O_{46}H_3]^{8-}$ species, which further condenses into oligomeric anions at lower pH values [51]. To our knowledge, there are only three examples of structurally characterized molecular hybrid borotungstates: the $[\{Ru(L)\}_2(HBW_{11}O_{39})_2WO_2]^{10-}$ (L = *p*-cymene, benzene) clusters based on the $\{HBW_{11}\}$ unit [52] and the dimethyltin-containing $[\{(CH_3)_2Sn\}_6(OH)_2O_2(H_2BW_{13}O_{46})_2]^{12-}$ anion showing $\{H_2BW_{13}\}$ subunits [53]. Although the insertion of organophosphonate groups in monolacunay borotungstates has been previously suggested [32], compound **TBA-1** reported herein represents the first example in the literature of a structurally characterized group-13 heteropolytungstate that is derivatized with organo-p-block moieties. The use of the topologically equivalent $[SiW_{11}O_{39}]^{8-}$ precursor in combination with 1-naphthylmethylphosphonic acid led to the isolation of the isostructural compound **TBA-2**.

The functionalization of the POM precursor was firstly identified by infrared spectroscopy (FT-IR). FT-IR spectra of compounds **TBA-1** and **TBA-2** are depicted in Figure 1 together with those of their corresponding $K_8[HBW_{11}O_{39}]\cdot 13H_2O$ ($\{HBW_{11}\}$) and $TBA_8[SiW_{11}O_{39}]$ ($\{SiW_{11}\}$) precursors. Both compounds exhibit characteristic bands of strong intensity in the region below 1000 cm^{-1} that are associated with monolacunary α-Keggin-type anions. The antisymmetric stretching vibrational bands ν_{as}(X–O_c), ν_{as}(W–O_t) and ν_{as}(W–O_b–W) at 1220, 971 and 734 cm^{-1} for **TBA-1** are shifted in comparison with those of $\{HBW_{11}\}$, which appear at 1236, 954 and 752 cm^{-1}, respectively. In the case of **TBA-2**, these signals are observed at 1028, 978, and 802 cm^{-1} and undergo blue shifts by *ca.* 10 cm^{-1} when compared with those of the parent $\{SiW_{11}\}$ anion. The presence of organophosphonate groups in both

compounds is confirmed by the signals associated with the stretching of the P–O bonds that appear in the 1060–1080 cm^{-1} range. The organic region above 1100 cm^{-1} is dominated by signals of medium to strong intensity that are observed in the 1176–1300 cm^{-1} range and associate with the C–N and C–H bonds from the TBA cations and the stretching vibrations of C=C bonds in the naphthalenic system. It is worth highlighting that the protonation of the central O atom in the borotungstate subunit of **TBA-1** can be unequivocally inferred by IR spectroscopy on the basis of the ν_{as}(B–O–H) vibrational band observed at 1220 cm^{-1}, which is red shifted by 20 cm^{-1} in comparison with that of the precursor [54].

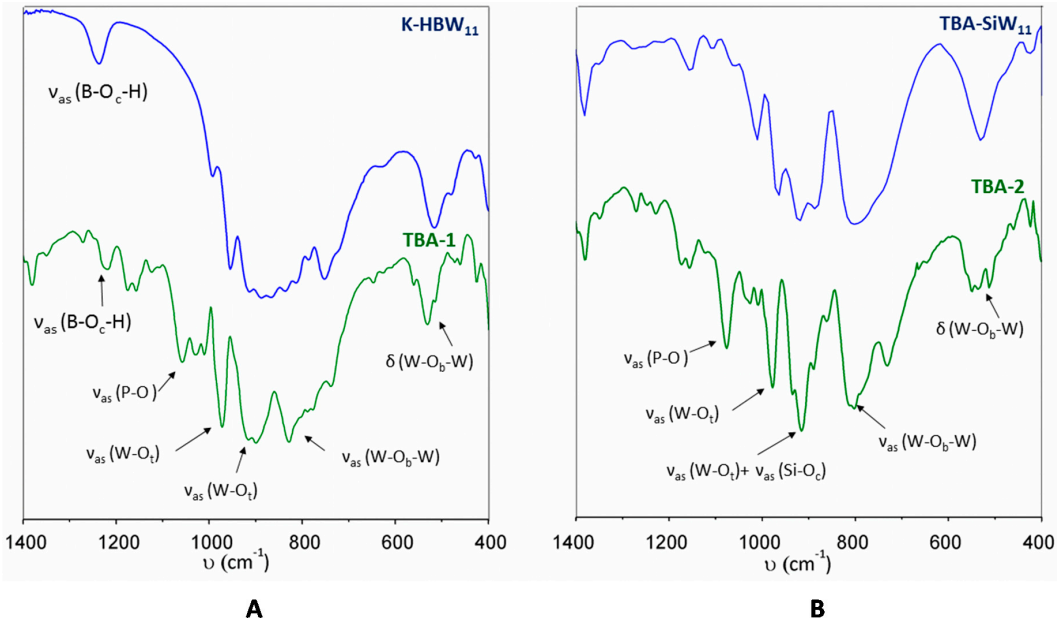

Figure 1. FT-IR spectra of **TBA-1** (**A**) and **TBA-2** (**B**) compared with those of their corresponding precursors $K_8[HBW_{11}O_{39}]\cdot 13H_2O$ and $TBA_8[SiW_{11}O_{39}]$.

Thermogravimetric analyses (TGA) show curves with similar profiles for both compounds (Figure S1). The wide thermal stability range, which extends up to *ca.* 280 °C for **TBA-1** and to *ca.* 290 °C for **TBA-2**, originates from the absence of any solvent molecules in the solid samples upon being left to dry overnight in air. The first weight loss is completed at 415 °C and comprises the loss of *ca.* 19% of the total mass, which accounts for the 3 tetrabutylammonium molecules (%mass, calcd. (found) for 3 × $C_{16}H_{36}N$: 19.33 (19.55) for **TBA-1** and 19.25 (19.08) for **TBA-2**). The final step, which corresponds to the organic ligand combustion and POM breakdown, extends continuously up to temperatures in the 800–850 °C range (%mass, calcd. (found) for two naphthylmethyl groups, 2 × $C_{11}H_9$: 8.33 (8.40) for **TBA-1** and 8.31 (8.25) for **TBA-1**). The final residues are 72.1% of the initial mass for **TBA-1** (calcd. for $HBP_2W_{11}O_{40}$: 72.7%) and 72.7% for **TBA-2** (calcd. for $P_2SiW_{11}O_{40}$: 72.8%).

2.2. Crystal Structure

Compounds **TBA-1** and **TBA-2** are isostructural and crystallize in the triclinic space group $P\bar{1}$ with two $[H(C_{11}H_9PO)_2(\alpha\text{-}H_nXW_{11}O_{39})]^{3-}$ (X = B, n = 1 (**1**); X = Si, n = 0 (**2**)) hybrid POMs and six tetrabutylammonium (TBA) cations in the asymmetric unit. Unfortunately, only five out of the six TBA cations could be satisfactorily modeled in the crystal structure of **TBA-2** due to severe crystallographic disorder, whereas the poorer quality of crystals of **TBA-1** only allowed us to locate one TBA ion. The molecular structures of the hybrid POMs **1** and **2** consist of a monolacunary α-Keggin-type anion that incorporates two 1-naphthylmethylphosphonate moieties in the vacant position as antenna ligands via corner-sharing of the phosphonate group with one $\{W_2O_{10}\}$ unit and one $\{W_3O_{13}\}$ trimer (Figure 2). The cluster shows idealized C_s symmetry with a mirror plane that contains the heteroatom and the bridging O atoms of the $\{W_2O_{10}\}$ unit (Figure 2B). This ideal symmetry is broken by the

relative arrangement of the naphthyl residues (Figure 2C). The planes containing the aromatic systems form angles in the 15°–25° range with the ideal mirror plane. However, both naphthyl residues from each of the POM units are arranged in a staggered conformation. The aromatic systems are rotated about 20° with respect to each other as defined by the <centroid···P···P···centroid> torsion angle involving equivalent ring centroids in both residues. As shown in Figure 2D, this orientation allows for establishing bifurcated intramolecular C–H···O_{POM} hydrogen bonds that involves the methylenic groups pointing towards the polyanionic surface and bridging O atoms from the POM unit (Table 1).

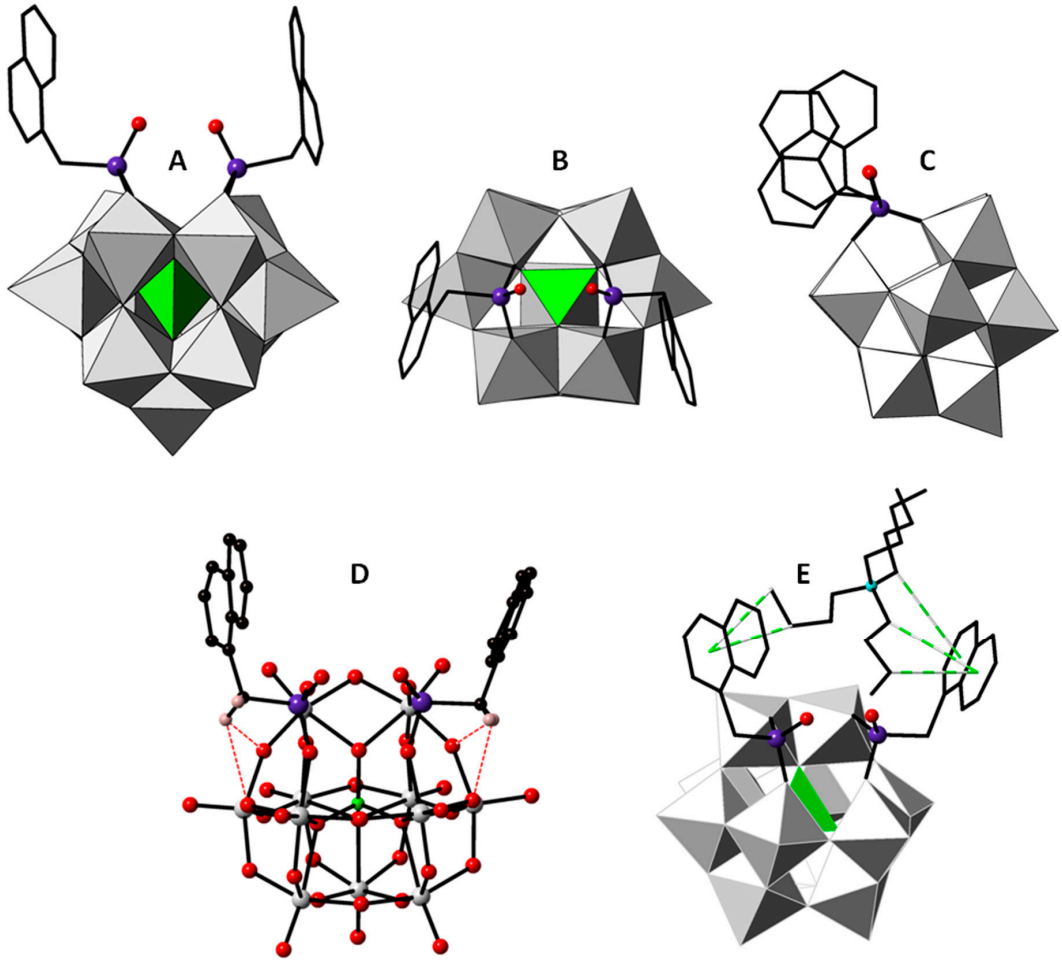

Figure 2. Polyhedral representation of the molecular structure of POMs **1** and **2** (**A**); The connectivity of the phosphonate groups and the relative arrangement of the naphthyl residues are highlighted in (**B**) and (**C**), respectively; Ball-and-stick representation of the hybrid POMs with intramolecular C–H···O_{POM} hydrogen bonds depicted in red dashed lines (**D**); Detail of the TBA cation embraced between the two aromatic systems via C–H···π interactions depicted as green dashed lines (**E**). Color code: WO_6, gray octahedra (W, gray); XO_4, green tetrahedra (X, green); P, violet; O, red; C, black; H, pink; N, cyan. Aromatic and *n*-butyl H atoms are omitted for clarity.

The P atoms are bonded to the methylenic C atom from the 1-naphthylmethyl moiety, two O atoms from the POM and one terminal O atom (Table S1), and this bonding scheme results in distorted tetrahedral geometries. Bond Valence Sum Calculations (BVS) [55] indicate partial protonation of the terminal O atoms in the phosphonate moieties (BVS values: 1.26–1.45) in good agreement with the number of cations determined by elemental and thermal analyses. One proton is disordered over the P=O bonds of the two organophosphonate groups for each of the hybrid POMs in the asymmetric unit. BVS calculations also indicate protonation of the central O_{POM} atom pointing toward

the vacant position in both crystallographically independent polyanions of compound **TBA-1** (BVS values: 1.15–1.17) and this fact is fully consistent with the presence of the B–O–H stretching band in the IR spectrum.

Table 1. Geometrical parameters (Å, °) for the intramolecular C–H···O hydrogen bonds involving the methylenic C atoms of the 1-naphthylmethylphosphonate groups and the O_{POM} atoms in compounds **TBA-1** and **TBA-2**.

D–H···A	H···A	D···A	<D–H···A>
TBA-1			
C1–H1B···O21	2.85	3.47(3)	121
C1–H1B···O28	2.71	3.32(3)	120
C21–H21A···O25	2.59	3.09(3)	111
C21–H21A···O31	2.63	3.29(3)	124
C201–H20B···O221	2.86	3.40(3)	115
C201–H20B···O228	2.81	3.47(3)	125
C221–H22A···O225	2.61	3.27(3)	123
C221–H22A···O231	2.63	3.11(3)	111
TBA-2			
C1–H1B···O21	2.46	3.05(5)	111
C1–H1B···O28	2.55	3.15(5)	127
C21–H21A···O25	2.77	3.46(4)	127
C21–H21A···O31	2.89	3.44(4)	115
C201–H20B···O221	2.86	3.52(4)	124
C201–H20B···O228	2.94	3.47(4)	115
C221–H22A···O225	2.52	3.04(5)	113
C221–H22A···O231	2.48	3.18(5)	127

The relative arrangement of the naphthyl residues allows the insertion of a bulky TBA cation (N1 and N4), in such a way that this results embraced between the two aromatic systems via nonconventional cation···π [56] and C–H···π type interactions [57] (Figure 2E). The distances of the C atoms from the TBA cations to the ring centroids (3.683(4)–4.188(6)Å) compare well with those calculated in the literature for such type of C–H···π contacts [58]. The crystal packing displays a pronounced two-dimensional character with hybrid anions linked through C–H···O_{POM} hydrogen bonds in bilayers that stack along the [001] direction. These bilayers comprise POM clusters located at z = 0.25 and z = 0.75, and arrange in such a way that each POM is connected to two neighbors of the same z level along the crystallographic y-axis and to another two in the contiguous hemilayer through a hydrogen bonding network involving the naphthyl groups (Figure 3, Table S2). The N1 and N4 TBA cations placed between naphthyl groups reinforce the connectivity within the bilayer. Moreover, the N3 and N5 cations connect POMs of the same z level in a zigzag mode along the [010] direction through an additional set of massive C–H···O_{POM} hydrogen bonds, whereas the remaining N2 species (and most likely the sixth undetermined TBA cation) occupy interlamellar spaces.

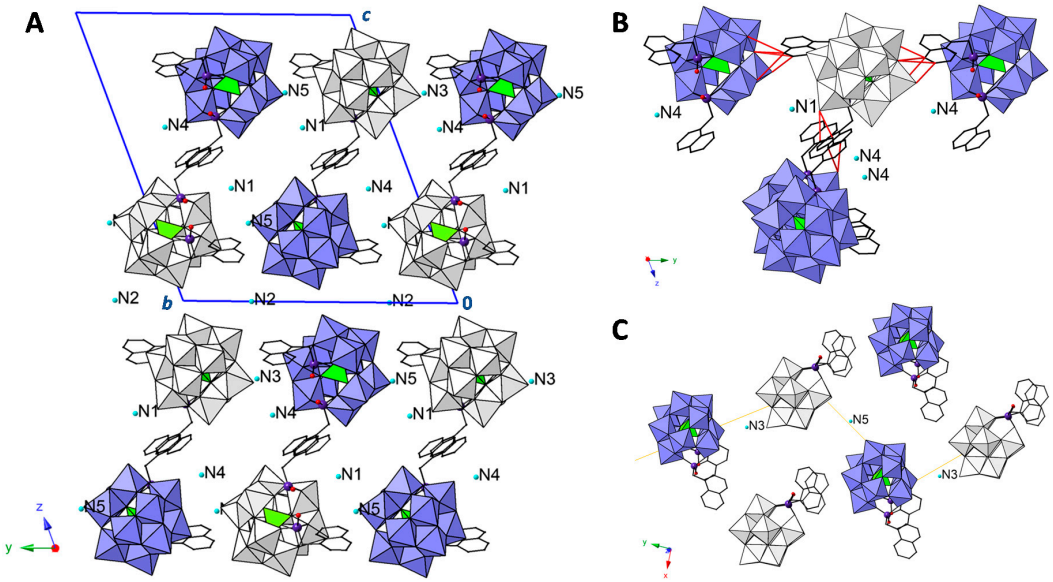

Figure 3. View of the crystal packing of compounds **TBA-1** and **TBA-2** along the [100] direction (**A**); Connectivity between POMs through intermolecular C–H···O_{POM} hydrogen bonds (depicted as red lines) within bilayers (**B**); Projection of a layer along the [001] direction where the N3 and N5 TBA cations connect POMs of the same *z* level in a zigzag mode (**C**). Color code: same as in Figure 2, crystallographically independent POM clusters are depicted in blue and gray. Butyl groups from TBA cations and aromatic H atoms are omitted for clarity.

2.3. UV–Vis Spectroscopy and Photoluminescent Properties

The electronic properties of the title compounds have been explored by both solution and diffuse reflectance UV–Vis spectroscopy. Figure 4 displays the UV–Vis spectra of acetonitrile solutions of **TBA-2** with different concentrations (c_1 = 10^{-4} M; c_2 ≈ 10^{-6} M; c_3 ≈ 10^{-8} M), together with those obtained for the 1-naphthylmethylphosphonic acid and the $TBA_8[SiW_{11}O_{39}]$ POM precursor, which has been prepared for comparative purposes following reported procedures [59]. The rapid transformation of $\{BW_{11}\}$ to $\{BW_{12}\}$ in slightly acidic aqueous medium precluded us from preparing the corresponding $TBA_8[HBW_{11}O_{39}]$ analogue to perform similar comparative studies for the **TBA-1** derivative. Methathesis with TBABr led to the isolation of the very stable plenary Keggin anion α-$[BW_{12}O_{40}]^{5-}$ as a TBA salt according to IR spectroscopy. Samples with different concentrations of the title compounds have been used for our studies due to the great differences in the relative intensity of the absorption bands.

The electronic spectrum of the parent $\{SiW_{11}\}$ precursor displays an absorption maximum at 265 nm that is associated with the O→W ligand-to-metal charge transfer (LMCT) transition of the inorganic POM framework. In turn, the 1-naphthylmethylphosphonic acid shows two absorption bands at 224 and 289 nm, which correspond to the well-known $\pi-\pi^*$ transitions of the naphthalenic system [60]. The former band is also present in the spectrum of **TBA-2** (see the spectrum of the 10^{-8} M solution) and is accompanied by a second broad absorption centered at 275 nm that originates from a small bathochromic shift of about 10 nm of the LMCT band upon functionalization of the monolacunary cluster with organophosphonate groups. Such type of bathochromic shift is indicative of an electronic transfer between the conjugated organic fragment and the metal-oxo cluster [61]. The spectrum recorded for the 10^{-6} M solution affords a better resolution in this spectral region. The absorption band is considerably wider than that observed for the LMCT transition in the parent $\{SiW_{11}\}$ precursor and it shows a shoulder at 283 nm that is in good correspondence with the naphthyl $\pi-\pi^*$ transitions observed for the phosphonic acid in this region. The combination of these two features strongly indicates that the absorption of **TBA-2** centered at 275 nm has a strong contribution of the naphthalenic system.

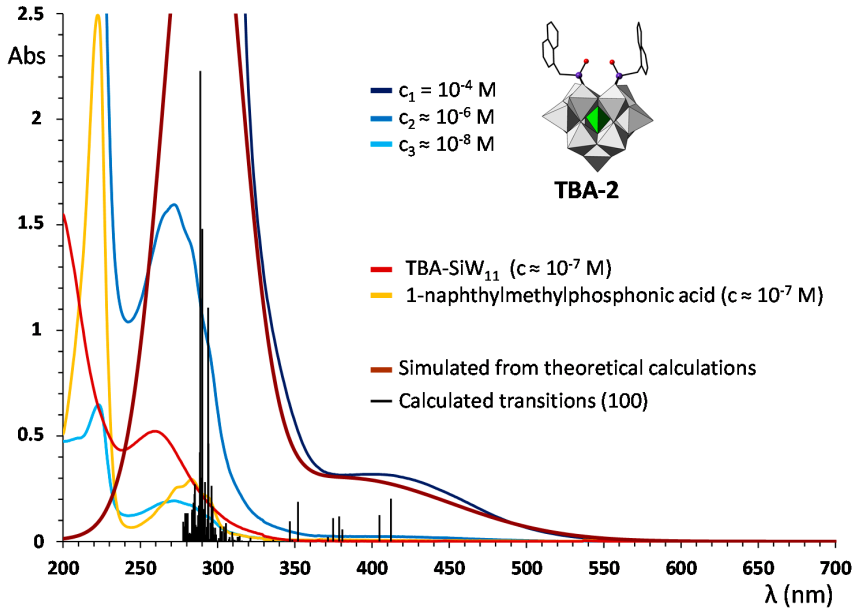

Figure 4. UV–Vis spectra of acetonitrile solutions of **TBA-2** with different concentrations compared with those of the commercial 1-naphthylmethylphosphonic acid and the $TBA_8[SiW_{11}O_{39}]$ precursor. The simulated spectrum from theoretical TD-DFT calculations and the first 100 transitions with calculated relative intensity are also depicted.

The spectrum of the concentrated solution of **TBA-2** shows and additional band centered at *ca.* 400 nm that could be ascribed to a charge transfer between the aromatic system and the inorganic POM cluster in which the former acts as electron donor and the latter as acceptor. This phenomenon has been previously observed for similar compounds in the literature [61,62]. The charge-transfer process can be noticed visually because the incorporation of the colorless 1-naphthylmethylphosphonate moiety into the inorganic skeleton of the colorless $\{SiW_{11}\}$ leads to the formation of the orange-yellow compound **TBA-2**. A similar behavior is observed in the UV–Vis spectra of **TBA-1** solutions (Figure S2). The bands at *ca.* 222 and 282 nm can be associated with the well-known $\pi-\pi^*$ transitions of the naphthyl residue, whereas that at 274 nm corresponds to the LMCT process. The maximum for the charge transfer band between the naphthyl residue and the inorganic POM cluster is blue-shifted by 15 nm upon comparison with that of **TBA-2** (*ca.* 385 nm in **1** *vs. ca.* 400 nm in **2**). Accordingly, crystals of compound **TBA-1** display a more yellowish color than those of **TBA-2** (Figure 5).

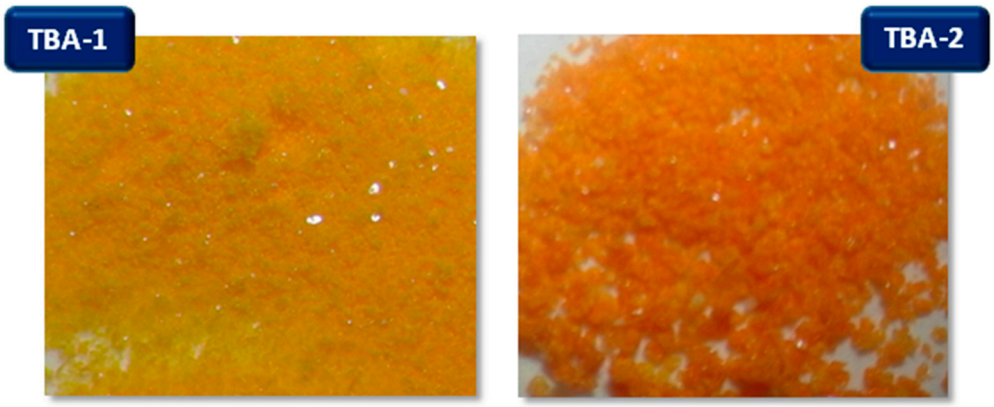

Figure 5. Photographs of the crystalline batches of **TBA-1** and **TBA-2** upon being left to dry in air overnight.

In order to analyze the nature of the band centered at *ca.* 400 nm, theoretical calculations for the hybrid POM **2** at the TDA-B3LYP/def2-SVP//BP86-D3/def2-SVP level of theory have been performed. They show qualitative agreement with the experimental results, with several low intensity transitions in the visible region (408, 380 and 350 nm) that fall under the very wide experimental band centered at 400 nm, as well as a cluster of higher intensity transitions centered at 290 nm (Figure 4). The difference density plots of the molecular orbitals involved in the low intensity bands clearly indicate their organic to inorganic charge transfer character, with the naphthalenic system acting as electron donor and the POM cluster as acceptor (W d_{xy} with a component of O p orbitals). On the other hand, the difference densities calculated for the cluster of transitions centered at 290 nm clearly support their previous assignment as O→W LMCT transition in the inorganic POM framework (Figure 6D) combined with $\pi-\pi^*$ transitions in the naphthyl groups (Figure 6E).

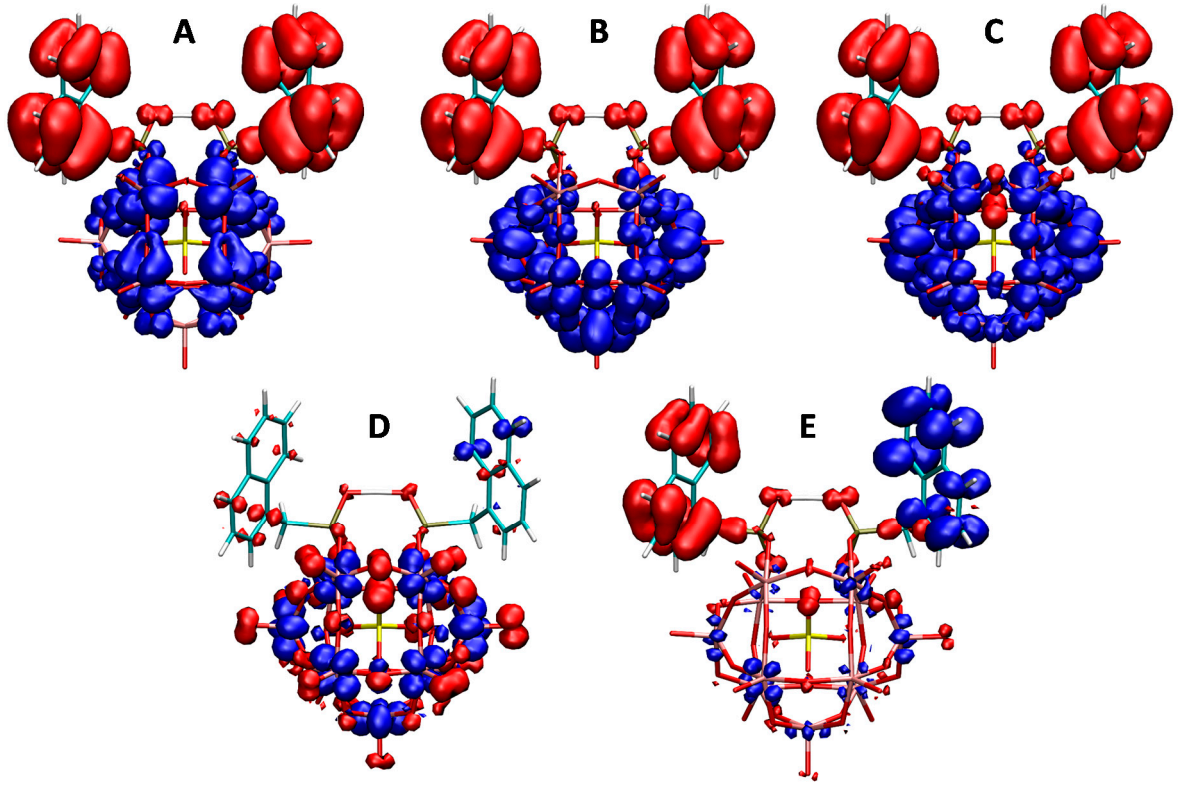

Figure 6. Difference densities for several CT transitions calculated for the hybrid POM **2** at the TDA-B3LYP/def2-SVP//BP86-D3/def2-SVP level of theory. The electronic transfer is from the red to the blue surfaces: (**A**) 408 nm; (**B**) 380 nm; (**C**) 350 nm; (**D**) 290 nm and (**E**) 290 nm.

The diffuse reflectance spectra registered for powdered crystalline samples of **TBA-1**, **TBA-2** and their precursors $K_8[HBW_{11}O_{39}]\cdot 13H_2O$ and $K_8[SiW_{11}O_{39}]\cdot 13H_2O$ (Figure 7) confirm the features stated from the solution studies. The bands associated with the monolacunary Keggin anions undergo red shift upon organic functionalization from 313 and 318 nm for the $\{HBW_{11}\}$ and $\{SiW_{11}\}$ POM precursors to 336 and 341 nm for the hybrid compounds **TBA-1** and **TBA-2**. Strong charge transfer bands originating from the covalent connection between the naphthyl moieties and the inorganic oxo-cluster can also be observed in the visible region.

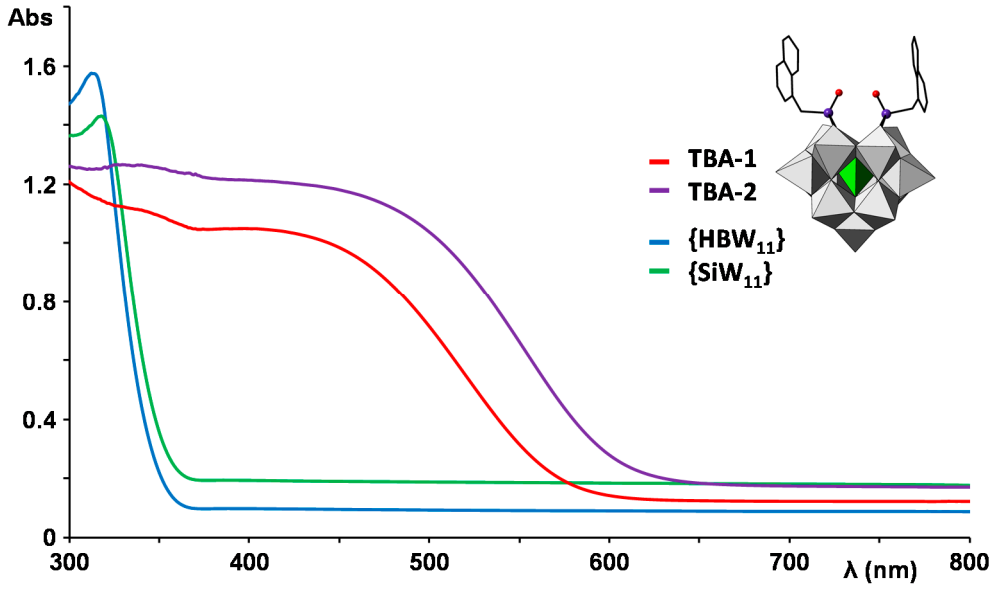

Figure 7. Diffuse Reflectance UV–Vis spectra of powdered crystalline samples of **TBA-1** and **TBA-2** compared with those of the $K_8[HBW_{11}O_{39}]\cdot 13H_2O$ and $K_8[SiW_{11}O_{39}]\cdot 13H_2O$ precursors.

Naphthalene and its derivatives present photoluminescent properties when they are excited with UV light [60]. To determine whether these emission properties are modified upon the incorporation of the 1-naphthylmethylphosphonate groups into monovacant Keggin anions, we measured the fluorescence spectra of 10^{-6} M acetonitrile solutions of the title compounds **TBA-1** and **TBA-2** and compared the results with that recorded for commercial 1-naphthylmethylphosphonic acid (Figure 8). The spectrum of the free phosphonic acid (λ_{exc} = 283 nm) shows a broad emission band with the typical naphthalenic vibrational structure in the *ca.* 300−400 nm spectral range. However, our hybrid polyanions **1** and **2** do not display any emission when being excited at any wavelength corresponding to their absorption maxima (225, 275 or 280 nm), nor even at the charge transfer band (385–400 nm). Similar results were obtained when the experiments were carried out on solid crystalline samples (Figure S3). Nevertheless, a weak fluorescence reminiscent of that originating from the naphthyl group was obtained when **1** and **2** were excited at 283 nm, but only when the spectrofluorimeter was set to work in a High Sensitivity mode. The quenching of the naphthalenic emission in the hybrid POMs **1** and **2** could result from two different processes: (i) the strong absorption of the Keggin-type cluster at the excitation wavelength (*ca.* 280 nm) prevents the excitation of the fluorophore; or (ii) the quenching of the fluorescence proceeds via naphthyl-to-cluster charge transfer. The former could in principle be disregarded according to the UV–Vis spectrum of **TBA-2** (Figure 4), which unequivocally shows that the naphthyl groups undergo strong absorption at 283 nm. Therefore, the quenching of the naphthyl fluorescence upon incorporation of the organophosphonate group into the Keggin-type skeleton is more likely to take place via naphthyl-to-POM charge transfer, which allows the excited state to deactivate through non-radiative processes. TD-DFT calculations support the latter interpretation as they clearly show that the naphthyl groups in the hybrid POMs **1** and **2** are excited in the 280–290 nm range (Figure 6D,E). Analogous quenching of the photoluminescent properties of aromatic systems such as pyrene upon incorporation into POM cluster frameworks has been previously reported in the literature for hybrid species similar to polyanions **1** and **2** [62].

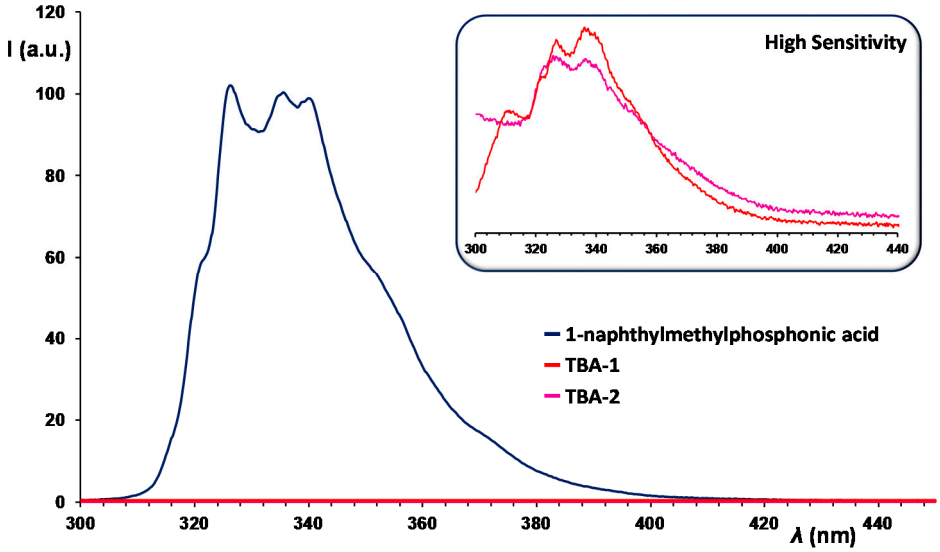

Figure 8. Fluorescence emission spectra of 10^{-6} M acetonitrile solutions of **TBA-1**, **TBA-2** and 1-naphthylmethylphosphonic acid in the 300–450 nm region (λ_{exc} = 283 nm).

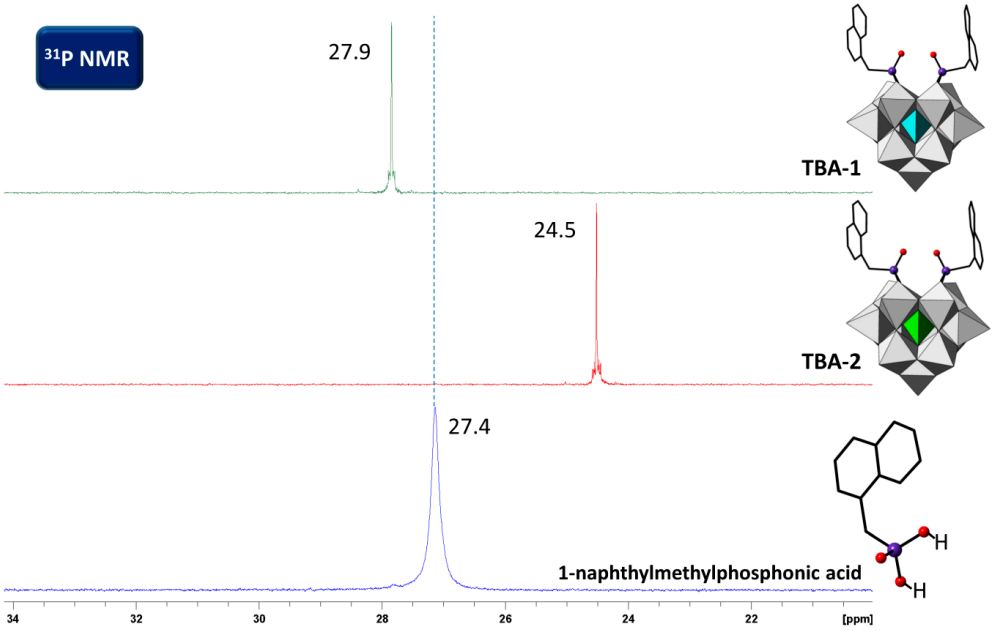

Figure 9. ^{31}P-NMR spectra of **TBA-1** and **TBA-2** in acetone-d_6 compared with that of the commercial 1-naphthylmethylphosphonic acid.

2.4. Solution Behavior

In order to investigate the solution stability of the hybrid POMs **1** and **2**, we performed ^{31}P-, ^{1}H- and ^{13}C-nuclear magnetic resonance (NMR) studies in deuterated solvents and compared the resulting spectra with that of the commercial 1-naphthylmethylphosphonic acid.

The ^{31}P-NMR spectra of compounds **TBA-1** and **TBA-2** in acetone (Figure 9) exhibit one singlet at 27.9 and 24.5 ppm, respectively. This fact indicates: (i) the absence of any phosphorous containing impurities in the sample; and (ii) that the attachment mode of the two organic groups to the lacunary anion is equivalent for both hybrid anions in good agreement with the molecular structures determined from single-crystal X-ray diffraction studies. All the chemical shifts lay in the expected range for organophosphonate derivatized monolacunary Keggin type POMs [63]. Depending on the heteroatom

of the Keggin-type fragment, the signal shifts considerably upfield (**2**, $\Delta\delta$ = 2.9 ppm) or slightly downfield (**1**, $\Delta\delta$ = 0.5 ppm) upon comparison with that originated from the parent commercial phosphonic acid (δ = 27.4 ppm).

The title compounds **TBA-1** and **TBA-2** display similar ^{1}H-NMR spectra that are depicted in Figure S4 together with that recorded for the naphthylmethylphosphonic acid. The grafting of the organophosphonate moiety could be confirmed by the absence of any signal corresponding to hydroxyl groups in the spectra of **TBA-1** and **TBA-2**, which for the phosphonic acid appears as a broad singlet at δ = 10.59 ppm that integrates for two protons. The characteristic resonances for the *n*-butyl groups of the TBA cations observed at *ca.* 1 (–C**H**$_3$), 1.5 (–C**H**$_2$–CH$_3$), 1.8 (–C**H**$_2$–CH$_2$–) and 3.4 (–N–C**H**$_2$–) ppm have been integrated for 36, 24, 24 and 24 protons, and this fact confirms the presence of three cations per POM unit. Protons in the aliphatic *n*-butyl chain are less shielded as they place closer to the N atom and show the expected spin coupling constant of J = 7.4 Hz [64]. The signals originating from the methylenic group of the organophosphonate moiety undergo drastic changes upon incorporation into the POM vacant position. The spin system, determined as two singlets at 3.47 and 3.51 ppm in the phosphonic acid, becomes diastereotopic in the hybrid POM structure in such a way that four different protons can be differentiated: H_a and H_b from one of the P(O)CH$_2$C$_{10}$H$_7$ moieties and H_c and H_d from the other one (Figure 10). These four resonances appear as doublets with a geminal coupling constant of about J = 15.2 Hz and arrange into two well-separated groups of signals because those that originate from the two H atoms pointing at the POM surface undergo significantly larger shift downfield due to the intramolecular C–H$\cdots$O$_{POM}$ interactions, which promote the deshielding of the protons [15] (H_a and H_c: $\Delta\delta$ = 0.69–0.76 ppm for **TBA-1** and $\Delta\delta$ = 0.62–0.66 ppm for **TBA-2**; H_b and H_d: $\Delta\delta$ = 0.42–0.47 ppm for **TBA-1** and $\Delta\delta$ = 0.34–0.38 ppm for **TBA-2**). It is also worth noting the roof effect of the signals, which is characteristic of almost overlapping resonances showing similar intensity. In regard to the naphthylic H atoms, the spectra of **TBA-1** and **TBA-2** show different multiplets in the δ = 7.35–8.29 ppm range that are analogous to those observed for the phosphonic acid in the δ = 7.41–8.12 ppm region. On the other hand, the singlet located at 4.80 ppm in the spectrum of **TBA-1** can only be ascribed to the protonation of the central O$_{POM}$ atom (B–O–H) in the vacant position of the cluster, which has also been observed in the IR spectrum and inferred from BVS calculations on the molecular structure of **1**. These results also suggest that the hybrid POMs **1** and **2** show solution stability in organic media like acetone.

The ^{13}C-NMR experiments were first carried out for deuterated acetone solutions (Figure S5). The TBA cations in compounds **TBA-1** and **TBA-2** could be easily assigned to singlets appearing at 14 (–**C**H$_3$), 20 (–**C**H$_2$–CH$_3$), 25 (–**C**H$_2$–CH$_2$–) and 59 (–N–**C**H$_2$–) ppm. The aromatic signals are observed in the 126–135 ppm region. Some of them appear as doublets due to the spin coupling with the close NMR active P nucleus (J = 3–11 Hz). The spectrum of the 1-naphthylmethylphosphonic acid is very similar to that observed for the hybrid POMs with an additional doublet at 32.2 ppm that is ascribed to the methylenic group, which shows a large ^{1}J = 137.5 Hz spin-coupling constant with the vicinal P atom. Unfortunately, the resonances corresponding to this group in compounds **TBA-1** and **TBA-2** were partially overlapped with the strong signal originating from the solvent and this fact prevented us from performing a full analysis. Therefore, the final ^{13}C-NMR spectra for compounds **TBA-1** and **TBA-2** were registered using solutions in deuterated acetonitrile (Figure 11). The TBA cations appear as three singlets at 13.9 (–**C**H$_3$), 20.4 (–**C**H$_2$–CH$_3$) and 24.4 (–**C**H$_2$–CH$_2$–) ppm and a resonance at 59.5 ppm for **TBA-1** and 59.3 ppm for **TBA-2** that corresponds to the C atoms covalently bonded to the N atoms. Close inspection of this resonance reveals an apparent triplet, which is most likely the result of three singlets arising from the three virtually identical but inequivalent TBA cations. The phosphonate groups are observed as follows: one doublet corresponding to the methylene group at *ca*. 59.4 ppm with ^{1}J = 134.1 Hz for **TBA-1** and ^{1}J = 138.3 Hz for **TBA-2**, together with a set of resonances spanning in the 126–135 ppm region. The positions for singlets and doublets of the aromatic region are virtually identical in both cases: 126.5 (J = 4.5 Hz), 126.6, 126.9, 128.5 (J = 4.5 Hz), 129.2, 129.5 (J = 11.0 Hz), 130.0 (J = 8.0 Hz), 133 (J = 5.5 Hz) and 135 (J = 2.5 Hz) ppm. The spin coupling constants of 11.0, 8.0, and <5.5 Hz have been tentatively assigned as ^{2}J, ^{3}J and ^{4}J, respectively.

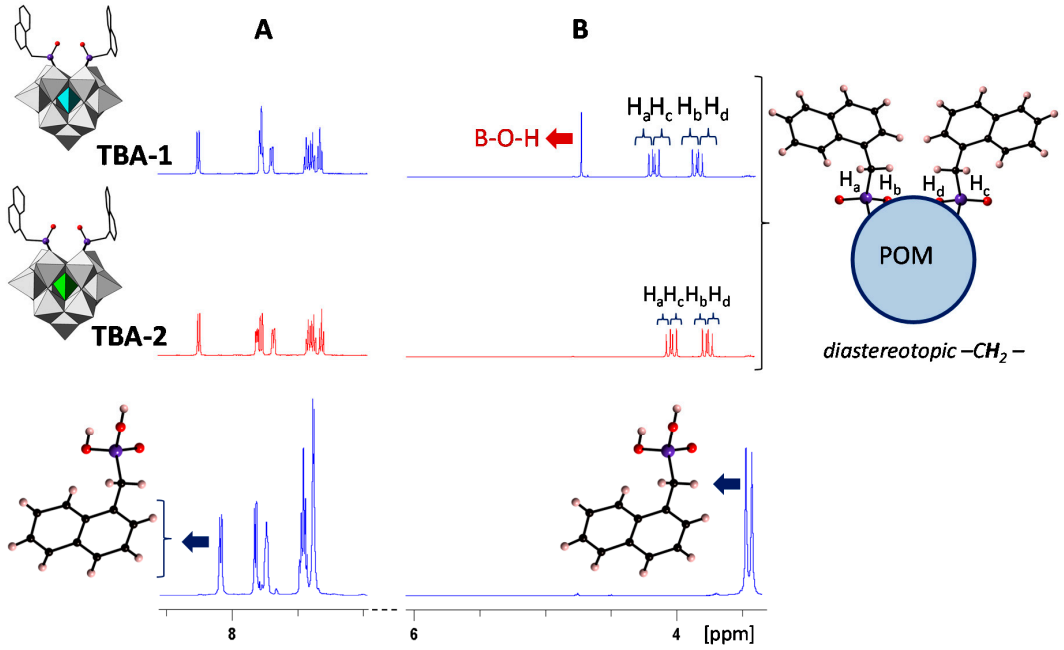

Figure 10. Expanded regions of the naphthyl (**A**) and methylenic (**B**) protons in the ^{1}H-NMR spectra of **TBA-1** and **TBA-2** recorded in acetone-d_6 compared with those of the commercial 1-naphthylmethylphosphonic acid. The diastereotopic spin system for the methylenic group in the hybrid POMs **1** and **2** is schematically depicted. The signal assigned to the B–O–H proton is highlighted in red.

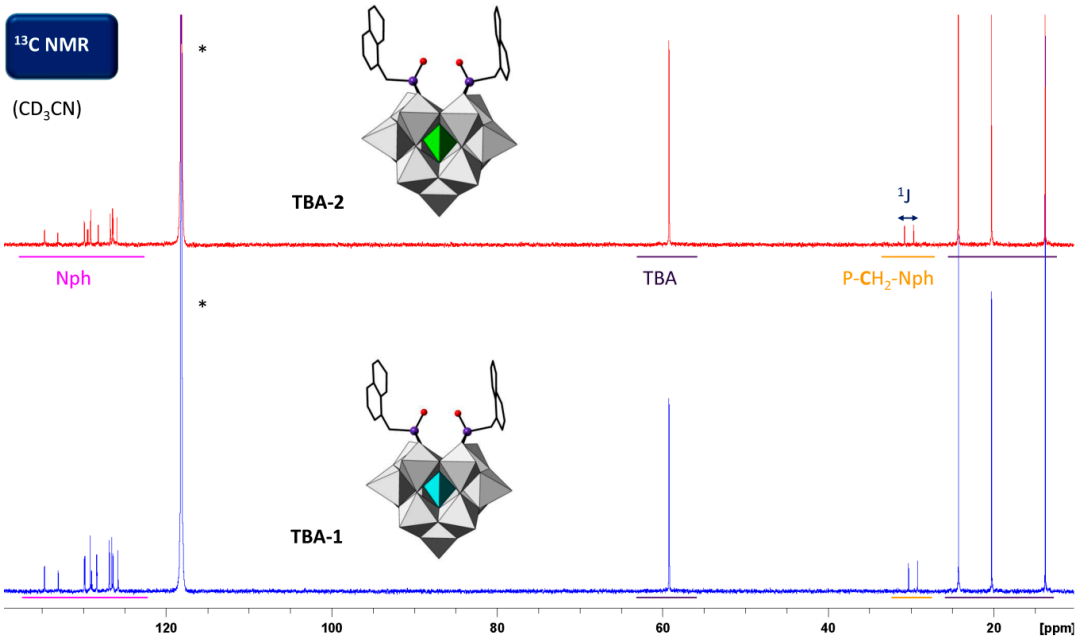

Figure 11. ^{13}C-NMR spectra of **TBA-1** and **TBA-2** in CD_3CN. The signals labeled as * correspond to the solvent.

The Electrospray-Ionization Mass Spectrometry (ESI-MS) studies confirm the solution stability of the hybrid polyanions **1** and **2**. The spectrum of **TBA-1** recorded in negative-ion mode displays two main groups of signals spanning from *m/z* 1000 to 1700. These signals have been attributed to the intact anionic species **1** with 3− and 2− charge states and different extents of associated counterions according to isotopic pattern inspection and *m/z* spacing. The main species detected corresponds to the pristine anion $\{\mathbf{1}\}^{3-}$ (*m/z* 1011.8), where $\{\mathbf{1}\}$ = $[H(C_{11}H_9PO)_2(HBW_{11}O_{39})]$, whereas the second

maxima originates from the intact species with an associated tetrabutylammonium cation, $\{\mathbf{1} + TBA\}^{2-}$ (*m/z* 1638.3). Figure 12 shows the ESI mass spectrum together with a comparison of the experimental and calculated isotopic patterns for these two specific ions. Inspection of the crystal structure of **1** revealed two protonation sites accounting for one disordered proton and the presence of one TBA cation embraced between the two naphthyl residues through multiple C–H$\cdots\pi$ type interactions. These two features could still be retained in solution according to the ESI-MS results. Analogous experiments carried out for the **TBA-2** derivative reveals a similar behavior. The most abundant species detected corresponds also to the intact hybrid anion $\{\mathbf{2}\}^{3-}$ (1017.4 *m/z*) and to the species with an associated TBA cation $\{\mathbf{2} + TBA\}^{2-}$ (*m/z* 1646.8) (Figure S6). To summarize, the combination of multinuclear (^{1}H, ^{13}C and ^{31}P) NMR studies and ESI-MS experiments confirms that the hybrid POMs **1** and **2** are stable in polar organic media like acetone or acetonitrile and do not dissociate into any of their constituent building blocks.

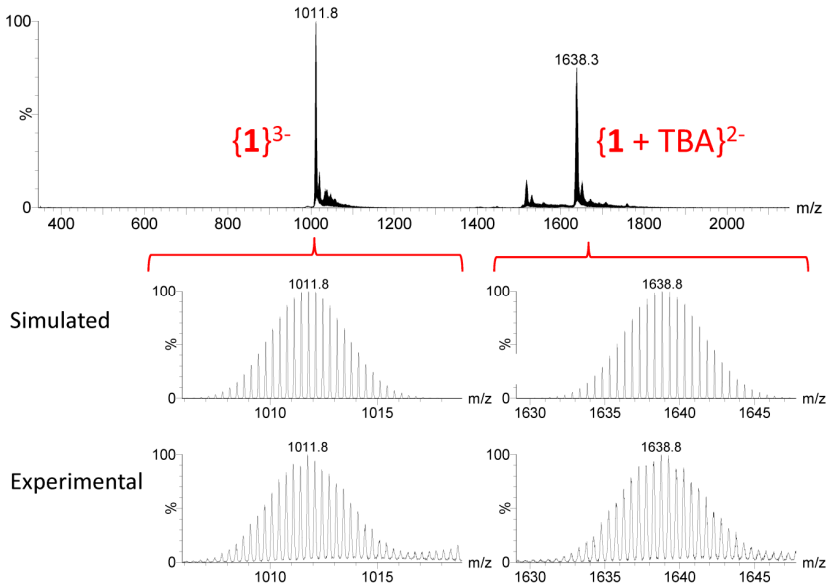

Figure 12. Negative ESI mass spectrum of a CH_3CN solution of **TBA-1** (U_c = 15 V) and comparison of the signals corresponding to the species $\{\mathbf{1}\}^{3-} = [H(C_{11}H_9PO)_2(HBW_{11}O_{39})]^{3-}$ and $\{\mathbf{1} + TBA\}^{2-} = \{(C_{16}H_{36}N)[H(C_{11}H_9PO)_2(HBW_{11}O_{39})]\}^{2-}$ with the simulated isotopic patterns.

3. Experimental Section

3.1. Materials and Methods

The precursors $K_8[\alpha\text{-}SiW_{11}O_{39}]\cdot 13H_2O$ and $K_8[\alpha\text{-}HBW_{11}O_{39}]\cdot 13H_2O$ were synthesized according to literature procedures [51,65] and identified by IR spectroscopy. All other reagents were purchased from commercial sources and used without further purification. Carbon, nitrogen, and hydrogen were determined on a EuroVector EA 3000 CHNSO analyzer (EuroVector, Milan, Italy). Fourier transform infrared (FT-IR) spectra were recorded on KBr pellets using a Shimadzu FTIR-8400S spectrophotometer (Shimadzu, Kyoto, Japan). Diffuse Reflectance studies were performed on a UV–Vis-NIR Varian Cary 500 spectrophotometer (Varian, Palo Alto, CA, USA). UV–Vis and fluorescence spectra were, respectively, registered on a Shimadzu UV-1240 spectrophotometer and a Shimadzu RF-5300 spectrofluorimeter equipped with a 150 W Xenon arc lamp (Shimadzu, Kyoto, Japan) using standard quartz cuvettes. Thermogravimetric analyses were carried out from room temperature to 850 °C at a rate of 5 °C$\cdot$ min^{-1} on a Mettler-Toledo TGA/SDTA851^e thermobalance (Mettler Toledo, Greifensee, Switzerland) under a 50 cm$^3\cdot$ min^{-1} flow of synthetic air. ^{1}H- and ^{13}C-NMR spectra were acquired on a Bruker AC-500 spectrometer (500 MHz for ^{1}H and 125.7 MHz for ^{13}C) (Bruker, Karlsruhe, Germany). Spectra were referenced to external tetramethylsilane via

the residual protonated solvent (^{1}H) or the solvent itself (^{13}C). All chemical shifts (δ) are reported in parts per million (ppm). For $(CD_3)_2CO$ (acetone-d_6) the shifts are referenced to 2.05 ppm for ^{1}H-NMR spectroscopy and 29.84 ppm for ^{13}C-NMR spectroscopy. For CD_3CN the shifts are referenced to 118.26 ppm for ^{13}C-NMR spectroscopy [66]. Abbreviations used in the description of resonances are: s (singlet), d (doublet), t (triplet), q (quartet), m (multiplet). Coupling constants (*J*) are quoted to the nearest 0.1 Hz. Proton-decoupled ^{31}P-NMR spectra were recorded on the same spectrometer working at 212.4 MHz using 85% phosphoric acid as internal standard (0 ppm). The ESI mass spectra for 10^{-5} M acetonitrile solutions were recorded in a Waters QTOF Premier instrument (Walters Corporation, Milford, MA, USA) with orthogonal Z-spray electrospray interface. The solution was introduced at a flow rate of 10 mL· min^{-1} and N_2 was used as the desolvation and cone gas (flow rates of 300 and 30 L· h^{-1}, respectively). A capillary voltage of 3.3 kV in the negative scan mode (V-mode) and relatively low cone voltages (U_c = 15 V) were used to control the extent of fragmentation of the gas-phase detected species.

*3.2. Synthesis of $[N(C_4H_9)_4]_3[H(C_{11}H_9PO)_2(HBW_{11}O_{39})]$ (**TBA-1**)*

To a suspension of $K_8[HBW_{11}O_{39}]\cdot 13H_2O$ (3.22 g, 1 mmol) in CH_3CN (50 mL) stirred at room temperature solid $[N(C_4H_9)_4]Br$ (1.605 g, 5 mmol) and $C_{11}H_9PO_3H_2$ (0.444 g, 2 mmol) were added. After 10 min, HCl 4 M (1 mL, 4 mmol) was added dropwise and the mixture was left overnight at reflux. Then, the insoluble white solid was removed by filtration and an orange powder was obtained by evaporation of the resulting solution in a rotary evaporator. The crude compound was washed with water and recrystallized from CH_3CN. Prismatic orange crystals of **TBA-1** suitable for X-ray diffraction were obtained upon slow evaporation of the final solution in an open vial for *ca.* 3 days. Yield: 2.33 g, 62% based on W. Elemental Analyses (%): calcd. (found) for $C_{70}H_{128}BN_3O_{41}P_2W_{11}$: C, 22.3 (23.0); H, 3.48 (3.71); N, 1.14 (1.15). IR (cm^{-1}): 3404 s, 2968 m, 2871 w, 1482 s, 1465 m, 1381 m, 1219 m,1176 w, 1155 w, 1058 s, 1029 s, 973 vs, 918 vs, 896 vs, 828 vs, 738 s, 560 w, 533 m, 425 w. ^{1}H-NMR (500 MHz, acetone-d_6): δ = 0.99 (36H, t, *J* = 7.4 Hz, –C**H**$_3$), 1.46 (24H, tq, *J* =7.4 Hz, 7.4 Hz, –C**H**$_2$–CH$_3$), 1.76–1.84 (24H, m, –C**H**$_2$–CH$_2$–), 3.36–3.43 (24H, m, –N–C**H**$_2$–), 3.89 (1H, d, *J* = 15.3 Hz, P(O)C**H$_a$**H$_b$), 3.94 (1H, d, *J* = 15.3 Hz, P(O)C**H$_c$**H$_d$), 4.22 (1H, d, *J* = 15.3 Hz, P(O)CH$_a$**H$_b$**), 4.27 (1H, d, *J* = 15.3 Hz, P(O)CH$_c$**H$_d$**), 4.80 (1H, s, B–O–**H**), 7.36 (2H, ddd, *J* = 8.3, 7.0, 1.1 Hz, C$_{arom}$**H**), 7.40–7.50 (4H, m, C$_{arom}$**H**), 7.73 (2H, dd, *J* = 8.3, 2.8 Hz, C$_{arom}$**H**), 7.78–7.84 (4H, m, C$_{arom}$**H**), 8.29 (2H, d, *J* = 8.3Hz, C$_{arom}$**H**) ppm. ^{13}C-NMR (CD_3CN): δ = 13.9 (s, –**C**H$_3$), 20.4 (s, –**C**H$_2$–CH$_3$), 24.4 (s, –**C**H$_2$–CH$_2$–), 29.9 (d, ^1J = 134.1 Hz, P(O)**C**H$_2$), 59.5 (s, –N–**C**H$_2$–), 125.9 (s, **C**$_{arom}$), 126.5 (d, *J* = 4.5 Hz, **C**$_{arom}$), 126.7 (s, **C**$_{arom}$), 127(s, **C**$_{arom}$), 128.5 (d, *J* = 4.5 Hz, C$_{arom}$), 129.1 (d, *J* = 11.4 Hz, **C**$_{arom}$), 129.3 (s, **C**$_{arom}$), 130.0 (d, *J* = 7.7 Hz, **C**$_{arom}$), 133.2 (d, *J* = 5.5 Hz, **C**$_{arom}$), 134.8 (d, *J* = 2.7 Hz, **C**$_{arom}$) ppm. ^{31}P-NMR (acetone-d_6): δ = 27.9 ppm.

*3.3. Synthesis of $[N(C_4H_9)_4]_3[H(C_{11}H_9PO)_2(SiW_{11}O_{39})]$ (**TBA-2**)*

The synthetic procedure above was followed but for using $K_8[SiW_{11}O_{39}]\cdot 13H_2O$ (3.22 g, 1 mmol) instead of $K_8[HBW_{11}O_{39}]\cdot 13H_2O$. Prismatic orange crystals of **TBA-2** suitable for X-ray diffraction were obtained upon slow evaporation of the final solution in an open vial for *ca.* 3 days. Yield: 2.12 g, 56% based on W. Elemental Analyses (%): calcd. (found) for $C_{70}H_{127}N_3O_{41}P_2SiW_{11}$: C, 22.3 (22.7); H, 3.49 (3.61); N, 1.14 (1.22). IR (cm^{-1}): 3430 s, 2965 m, 2873 w, 1642 m, 1479 w, 1376 w, 1176 w, 1155 w, 1078 s, 978 vs, 936 s, 918 vs, 889 s, 853 m, 731 s, 550 w, 531 w, 423 w. ^{1}H-NMR (500 MHz, acetone-d_6): δ = 0.98 (36H, t, *J* = 7.4 Hz, –C**H**$_3$), 1.45 (24H, tq, *J* = 7.4 Hz, 7.4 Hz, –C**H**$_2$–CH$_3$), 1.73–1.84 (24H, m, –C**H**$_2$–CH$_2$–), 3.30–3.44 (24H, m, –N–C**H**$_2$–), 3.81 (1H, d, *J* = 15.2 Hz, P(O)C**H$_a$**H$_b$), 3.85 (1H, d, *J* = 15.2 Hz, P(O)C**H$_c$**H$_d$), 4.08 (1H, d, *J* = 15.2 Hz, P(O)CH$_a$**H$_b$**), 4.13 (1H, d, *J* = 15.2 Hz, P(O)CH$_c$**H$_d$**), 7.35 (2H, ddd, *J* = 8.3, 7.0, 1.1 Hz, C$_{arom}$**H**), 7.38–7.48 (4H, m, C$_{arom}$**H**), 7.72 (2H, dd, *J* = 8.3, 2.8 Hz, C$_{arom}$**H**), 7.82–7.89 (4H, m, C$_{arom}$**H**), 8.28 (2H, d, *J* = 8.3 Hz, C$_{arom}$**H**) ppm. ^{13}C-NMR (CD_3CN): δ = 13.9 (s, –**C**H$_3$), 20.4 (s, –**C**H$_2$–CH$_3$), 24.4 (s, –**C**H$_2$–CH$_2$–), 30.3 (d, ^1J = 138.3 Hz, P(O)**C**H$_2$), 59.3 (s, –N–**C**H$_2$–), 126.0 (s, **C**$_{arom}$), 126.5 (d, *J* = 4.5 Hz, **C**$_{arom}$), 126.6 (s, **C**$_{arom}$), 128.3 (d, *J* = 4.5 Hz, **C**$_{arom}$), 129.2 (s, **C**$_{arom}$), 129.5 (d, *J* = 10.9 Hz, **C**$_{arom}$), 130.0 (d, *J* = 8.0 Hz, **C**$_{arom}$), 133.2 (d, *J* = 5.8 Hz, **C**$_{arom}$), 134.8 (d, *J* = 2.5 Hz, **C**$_{arom}$) ppm. ^{31}P-NMR (acetone-d_6): δ = 24.5 ppm.

3.4. X-ray Crystallography

Crystallographic data for compounds **TBA-1** and **TBA-2** are summarized in Table 2. Intensity data for compound **TBA-2** were collected at 100(2) K on an Agilent Technologies SuperNova diffractometer (Agilent Technologies Inc., Santa Clara, CA, USA) equipped with an Eos CCD detector and mirror-monochromated Mo *Kα* radiation (λ = 0.71073 Å). The data acquisition for compound **TBA-1** was carried out at 150(2) K using mirror monochromated Cu *Kα* radiation (λ = 1.54184 Å) and an Atlas CCDC detector. Data collections, unit cell determinations, intensity data integrations, routine corrections for Lorentz and polarization effects, and analytical absorption corrections with face indexing were performed using the CrysAlis Pro software package (Agilent Technologies UK Ltd., Oxford, UK) [67]. The structures were solved using OLEX2 (OlexSys Ltd in Durham University, Durham, UK) [68] and refined by full-matrix least-squares with SHELXL-97 (University of Göttingen, Göttingen, Germany) [69]. Final geometrical calculations were carried out with PLATON (Utrecht University, Utrecht, The Netherlands) [70] as integrated in WinGX (University of Glasgow, Glasgow, UK) [71]. Bond valence sum (BVS) calculations [55] were performed using the BVSumCalc program (courtesy of Michael H. Dickman). Thermal vibrations were treated anisotropically for atoms contained in the hybrid-POM framework (W, Si, O). All the bond lengths and isotropic thermal ellipsoids for aromatic and alkyl groups were normalized using SADI and SIMU-type restraints from SHELXL due to the considerable structural disorder. For the aromatic systems, some of the 1,3-distances (*i.e.*, distances between two atoms that are both bonded to the same atom, or "angle distances") were restrained to 2.42(2) Å. Hydrogen atoms of the 1-napththylmethyl groups and the methylenic carbons of the *n*-butyl chains were placed in calculated positions using standard SHELXL parameters. The H atoms of the $-CH_3$ carbons in the *n*-butyl chains were added as idealized methyl groups with staggered geometry (AFIX33) for the refinement to converge.

Table 2. Crystallographic data for **TBA-1** and **TBA-2**.

Parameters	TBA-1	TBA-2
Formula	$C_{70}H_{128}BN_3O_{41}P_2W_{11}$	$C_{70}H_{127}N_3O_{41}P_2SiW_{11}$
FW ($g\cdot mol^{-1}$)	3762.8	3779.1
Crystal System	Triclinic	Triclinic
Space Group	$P-1$	$P-1$
a (Å)	17.4020(5)	16.9676(5)
b (Å)	24.2390(3)	24.3022(3)
c (Å)	28.6175(5)	28.5333(7)
α (°)	70.095(2)	70.030(2)
β (°)	72.336(2)	72.703(2)
γ (°)	89.976(2)	89.957(2)
V ($Å^3$)	10743.3(4)	10491.3(4)
Z	4	4
ρ_{calcd} ($g\cdot cm^{-3}$)	2.326	2.393
μ (mm^{-1})	22.022	12.124
T (K)	150(2)	100(2)
λ (Å)	1.54184 (Cu *Kα*)	0.71073 (Mo *Kα*)
Collected Reflections	80334	65644
Unique Reflections (R_{int})	38193 (0.126)	36457 (0.048)
Observed Reflections [$I > 2\sigma(I)$]	23423	21696
Parameters/Restraints	767/250	1459/546
$R(F)^a$ [$I > 2\sigma(I)$]	0.095	0.083
$wR(F^2)^a$ [all data]	0.270	0.216
GoF	0.964	1.078

[a] $R(F) = \Sigma||F_o - F_c||/\Sigma|F_o|$; $wR(F^2) = \{\Sigma[w(F_o{}^2 - F_c{}^2)2]/\Sigma[w(F_o{}^2)^2]\}^{1/2}$.

Only five out of the six TBA counterions per two POM clusters determined by TGA, NMR and elemental analyses were located in the Fourier map of **TBA-2**. A sixth cation was found to be disordered over two positions, but it could not be successfully modeled. The much poorer quality of the crystals of **TBA-1** only allowed us to model one of the six TBA cations in the asymmetric unit. Therefore, the final structural models contained large solvent accessible voids accounting for *ca*. 55% (**TBA-1**) and 20% (**TBA-2**) of the unit cell that have been analyzed using the SQUEEZE tool of PLATON. The void of 5898 Å^3 in **TBA-1** is located at (x, y, z) = (0, 0, 0) and corresponds to 3301 electrons, whereas that of 2209 Å^3 in **TBA-2** is located at (x, y, z) = (1/2, 1/2, 0) and accounts for 1299 electrons. The calculated void could easily host the undetermined 2 TBA cations in the unit cell of **TBA-2**, which occupy *ca.* 1800 Å^3 if they are considered as spherical units with a radius of 6 Å. The remaining void space could be occupied by solvent molecules that are rapidly lost upon the exposure of the crystals at ambient conditions. In the case of **TBA-1**, the rough approximation used for estimating the volume occupied by the undetermined cations is inaccurate for such a large void accounting for more than the 50% of the unit cell. The hkl reflection file generated with SQUEEZE contained 23,423 (**TBA-1**) and 21,696 (**TBA-2**) observed reflections out of the 25,376 and 22,761 reflections in the original files. Refinement of the structural model using the squeeze-generated reflection file led to a significant improvement of the final R and wR^2 agreement factors in comparison to the original ones [**TBA-1**: R, 0.138 and wR^2 (all), 0.396; **TBA-2**: R, 0.107 and wR^2 (all), 0.247]. CCDC-1471565 (**TBA-1**) and 1471564 (**TBA-2**) contain the supplementary crystallographic data for this paper. These data can be obtained free of charge from The Cambridge Crystallographic Data Centre via www.ccdc.cam.ac.uk/data_request/cif.

3.5. Computational Details

All TD-DFT calculations were carried out with ORCA 3.0.3 software [72]. The geometry of the $[H(C_{11}H_9PO)_2(\alpha\text{-}SiW_{11}O_{39})]^{3-}$ anion, taken from the crystal structure of **TBA-2**, was optimized using the BP86 [73,74] generalized-gradient-approximation density functional, modified with Grimme's DFT-D3 atom-pairwise dispersion correction [75] with Becke–Johnson damping [76] to take into account London-dispersion effects. The Ahlrichs' double-ζ AO basis set with one set of polarization functions (def2-SVP) [77] was used for all atoms. The Stuttgart–Dresden quasi-relativistic effective core potential SD(60,MWB) [78] was applied to W atoms. The UV–Vis absorption spectrum was calculated (at the optimized geometry) using linear-response time-dependent density functional calculations (TD-DFT) within the Tamm–Dancoff approximation [79], with the same basis sets and ECPs as during geometry optimization, and using the B3LYP hybrid density functional [80]. In order to speed up the calculation, the essentially linear RIJCOSX approximation [81,82] has been used, which has been shown to lead to virtually no loss of accuracy [83].

4. Conclusions

The study presented herein represents a solid confirmation of the fact that the classical approach to functionalize lacunary POM clusters with organo-derivatives of the p-block can be applied to new platforms belonging to heteropolyoxotungstates with heteroatoms of the group 13. In this work, an organophosphonate derivative of a Keggin-type borotungstate (**TBA-1**) has been structurally characterized for the first time. Experiments carried out using the monolacunary Keggin-type silicotungstate have resulted in the hybrid **TBA-2** analogue and demonstrate that the functionalization with organophosphonate precursors such as 1-naphthylmethylphosphonic acid can be extended to isoelectronic POM species regardless of the different reactivity conferred by the heteroatoms. The UV–Vis spectroscopy reveals the presence of a charge transfer process promoted by transitions from the naphthyl aromatic system to the Keggin anion as confirmed by TD-DFT calculations. This electronic feature could be at the origin of the quenching that the fluorescent properties of the 1-naphthylmethylphosphonate group undergo upon its incorporation into the inorganic oxo-tungstate skeleton. A combination of multinuclear NMR studies and ESI-MS spectrometry confirms the solution stability of the hybrid frameworks in the organic media. We plan to react the obtained hybrid POM

platforms with catalytically active 3d- and 4f-metals centers in the near future with the aim of preparing models for supported site-isolated catalysts with an aromatic environment that will confer photoactive properties on the system and might enhance the selectivity of the catalytic process by interacting with the substrates and providing steric hindrance.

Supplementary Materials: The following supplementary materials are available online at www.mdpi.com/2304-6740/4/2/14/s1, Figure S1: TGA curves for **TBA-1** and **TBA-2**, Table S1: Bond lengths and angles for the P atoms in **TBA-1** and **TBA-2**, Table S2: Geometrical parameters for the intermolecular C–H···O hydrogen bonds involving 1-naphthylmethylphosphonate groups and O_{POM} atoms in **TBA-1** and **TBA-2**, Figure S2: UV–Vis spectra of acetonitrile solutions of **TBA-1** with different concentrations, Figure S3: Fluorescence emission spectra of solid samples of **TBA-1**, **TBA-2** and 1-naphthylmethylphosphonic acid in the 300–450 nm region (λ_{exc} = 283 nm), Figure S4: ^{1}H-NMR spectra of **TBA-1** and **TBA-2** in acetone-d_6 compared with that of the commercial 1-naphthylmethylphosphonic acid, Figure S5: ^{13}C-NMR spectra of **TBA-1** and **TBA-2** in acetone-d_6 compared with that of the commercial 1-naphthylmethylphosphonic acid, Figure S6: Negative ESI mass spectrum of a CH_3CN solution of **TBA-2** (U_c = 15 V) with details of the signals corresponding to the species $\{\mathbf{2}\}^{3-}$ = $[H(C_{11}H_9PO)_2(SiW_{11}O_{39})]^{3-}$ and $\{\mathbf{2} + TBA\}^{2-}$ = $\{(C_{16}H_{36}N)[H(C_{11}H_9PO)_2(SiW_{11}O_{39})]\}^{2-}$ compared with the simulated isotopic patterns.

Acknowledgments: This work was funded by the Spanish Ministerio de Economía y Competitividad (grant MAT2013-48366-C2-2P). The authors thank Cristian Vicent (Serveis Centrals d'Instrumentació Científica, Universitat Jaume I) for the ESI-MS experiments. Technical and human support provided by SGIker (UPV/EHU) is gratefully acknowledged.

Author Contributions: Nerea Andino prepared the title compounds and performed its physicochemical characterization in close collaboration with Beñat Artetxe and Santiago Reinoso; Leire San Felices collected the single-crystal X-ray diffraction data and solved the structures; Pablo Vitoria carried out the theoretical calculations; Santiago Reinoso and Beñat Artetxe prepared the manuscript and acted as scientific coordinators; Jose I. Martínez analyzed the NMR spectra; Fernando López Arbeloa and Beñat Artetxe were in charge of conducting the solution UV–Vis and fluorescence spectra; and Juan M. Gutiérrez-Zorrilla conceived the work.

Conflicts of Interest: The authors declare no conflict of interest.

References

1. Pope, M.T. *Heteropoly and Isopoly Oxometalates*; Springer: Berlin, Germany, 1983.
2. *Polyoxometalates: From Platonic Solids to Anti-Retroviral Activity*; Pope, M.T., Müller, A., Eds.; Kluwer: Dordrecht, The Netherlands, 1994.
3. *Polyoxometalate Chemistry: Some Recent Trends*; Sécheresse, F., Ed.; World Scientific: Singapore, 2013.
4. Gouzerh, P.; Proust, A. Main-group element, organic, and organometallic derivatives of polyoxometalates. *Chem. Rev.* **1998**, *98*, 77–111. [CrossRef] [PubMed]
5. Long, D.-L.; Tsunashima, R.; Cronin, L. Polyoxometalates: Building blocks for functional nanoscale systems. *Angew. Chem. Int. Ed.* **2010**, *49*, 1736–1758. [CrossRef] [PubMed]
6. Proust, A.; Thouvenot, R.; Gouzerh, P. Functionalization of polyoxometalates: Towards advanced applications in catalysis and materials science. *Chem. Commun.* **2008**, 1837–1852. [CrossRef] [PubMed]
7. Song, Y.-F.; Tsunashima, R. Recent advances on polyoxometalate-based molecular and composite materials. *Chem. Soc. Rev.* **2010**, *41*, 7384–7402. [CrossRef] [PubMed]
8. Santoni, J.-P.; Hanan, G.S.; Hasenknopf, B. Covalent multi-component systems of polyoxometalates and metal complexes: Toward multi-functional organic–inorganic hybrids in molecular and material sciences. *Coord. Chem. Rev.* **2014**, *281*, 64–85. [CrossRef]
9. Proust, A.; Matt, B.; Villanneau, R.; Guillemot, G.; Gouzerh, P.; Izzet, G. Functionalization and post-functionalization: A step towards polyoxometalate-based materials. *Chem. Soc. Rev.* **2012**, *41*, 7605–7622. [CrossRef] [PubMed]
10. Dolbecq, A.; Dumas, E.; Mayer, C.R.; Mialane, P. Hybrid organic–inorganic polyoxometalate compounds: From structural diversity to applications. *Chem. Rev.* **2010**, *110*, 6009–6048. [CrossRef] [PubMed]
11. Blazevic, A.; Rompel, A. The Anderson–Evans polyoxometalate: From inorganic building blocks via hybrid organic–inorganic structures to tomorrows "Bio-POM". *Coord. Chem. Rev.* **2016**, *307*, 42–64. [CrossRef]
12. Yin, P.; Wu, P.; Xiao, Z.; Li, D.; Bitterlich, E.; Zhang, J.; Cheng, P.; Vezenov, D.V.; Liu, T.; Wei, Y. A double-tailed fluorescent surfactant with a hexavanadate cluster as the head group. *Angew. Chem. Int. Ed.* **2011**, *50*, 2521–2522. [CrossRef] [PubMed]

13. Pradeep, C.P.; Long, D.-L.; Newton, G.N.; Song, Y.-F.; Cronin, L. Supramolecular metal oxides: Programmed hierarchical assembly of a protein-sized 21 kDa $[(C_{16}H_{36}N)_{19}\{H_2NC(CH_2O)_3P_2V_3W_{15}O_{59}\}_4]^{5-}$ polyoxometalate assembly. *Angew. Chem. Int. Ed.* **2008**, *47*, 4388–4391. [CrossRef] [PubMed]
14. Peng, Z. Rational synthesis of covalently bonded organic–inorganic hybrids. *Angew. Chem. Int. Ed.* **2004**, *43*, 930–935. [CrossRef] [PubMed]
15. Artetxe, B.; Reinoso, S.; San Felices, L.; Vitoria, P.; Pache, A.; Martín-Caballero, J.; Gutiérrez-Zorrilla, J.M. Functionalization of Krebs-Type polyoxometalates with *N*,*O*-chelating ligands: A systematic study. *Inorg. Chem.* **2015**, *54*, 241–252. [CrossRef] [PubMed]
16. Rousseau, G.; Oms, O.; Dolbecq, A.; Marrot, J.; Mialane, P. Route for the elaboration of functionalized hybrid 3d-substituted trivacant Keggin anions. *Inorg. Chem.* **2011**, *50*, 7376–7378. [CrossRef] [PubMed]
17. Fang, X.; Anderson, T.M.; Hill, C.L. Enantiomerically pure polytungstates: Chirality transfer through zirconium coordination centers to nanosized inorganic clusters. *Angew. Chem. Int. Ed.* **2005**, *44*, 3540–3544. [CrossRef] [PubMed]
18. Zheng, S.-T.; Zhang, J.; Yang, G.-Y. Designed synthesis of POM–organic frameworks from $\{Ni_6PW_9\}$ building blocks under hydrothermal conditions. *Angew. Chem. Int. Ed.* **2008**, *47*, 3909–3913. [CrossRef] [PubMed]
19. Zonnevijlle, F.; Pope, M.T. Attachment of organic groups to heteropoly oxometalate anions. *J. Am. Chem. Soc.* **1979**, *101*, 2731–2732. [CrossRef]
20. Kortz, U.; Hussain, F.; Reicke, M. The ball-shaped heteropolytungstates $[\{Sn(CH_3)_2(H_2O)\}_{24}\{Sn(CH_3)_2\}_{12}(A\text{-}XW_9O_{34})_{12}]^{36-}$. *Angew. Chem. Int. Ed.* **2005**, *44*, 3773–3777. [CrossRef] [PubMed]
21. Boglio, C.; Micoine, K.; Derat, E.; Thouvenot, R.; Hasenknopf, B.; Thorimbert, S.; Lacôte, E.; Malacria, M. Regioselective activation of oxo ligands in functionalized Dawson polyoxotungstates. *J. Am. Chem. Soc.* **2008**, *130*, 4553–4561. [CrossRef] [PubMed]
22. Nomiya, K.; Togashi, Y.; Kasahara, Y.; Aoki, S.; Seki, H.; Noguchi, M.; Yoshida, S. Synthesis and structure of Dawson polyoxometalate-based, multifunctional, inorganic–organic hybrid compounds: Organogermyl complexes with one terminal functional group and organosilyl analogues with two terminal functional groups. *Inorg. Chem.* **2011**, *50*, 9606–9619. [CrossRef] [PubMed]
23. Piedra-Garza, L.F.; Dickman, M.H.; Moldovan, O.; Breuning, H.J.; Kortz, U. Organoantimony-containing polyoxometalate: $[\{PhSbOH\}_3(A\text{-}\alpha\text{-}PW_9O_{34})_2]^{9-}$. *Inorg. Chem.* **2009**, *48*, 411–413. [CrossRef] [PubMed]
24. Knoth, W.H. Derivatives of heteropolyanions. 1. Organic derivatives of $W_{12}SiO_{40}{}^{4-}$, $W_{12}PO_{40}{}^{3-}$, and $Mo_{12}SiO_{40}{}^{4-}$. *J. Am. Chem. Soc.* **1979**, *101*, 759–760. [CrossRef]
25. Judeinstein, P.; Deprunb, C.; Nadjo, L. Synthesis and multispectroscopic characterization of organically modified polyoxometalates. *Dalton Trans.* **1991**, 1991–1997. [CrossRef]
26. Mayer, C.R.; Roch-Marchal, C.; Lavanant, H.; Thouvenot, R.; Sellier, N.; Blais, J.-C.; Sécheresse, F. New organosilyl derivatives of the Dawson polyoxometalate $[\alpha_2\text{-}P_2W_{17}O_{61}(RSi)_2O]^{6-}$: Synthesis and mass spectrometric investigation. *Chem. Eur. J.* **2004**, *10*, 5517–5523. [CrossRef] [PubMed]
27. Mazeaud, A.; Ammari, N.; Robert, F.; Thouvenot, R. Coordination chemistry of polyoxometalates: Rational synthesis of the mixed organosilyl derivatives of trivacant polyoxotungstates α-A-$[PW_9O_{34}(t\text{BuSiO})_3(RSi)]^{3-}$ and α-B-$[AsW_9O_{33}(t\text{BuSiO})_3(HSi)]^{3-}$. *Angew. Chem. Int. Ed. Engl.* **1996**, *35*, 1961–1964. [CrossRef]
28. Mayer, C.R.; Fournier, I.; Thouvenot, R. Bis- and tetrakis(organosilyl) decatungstosilicate, $[\gamma\text{-}SiW_{10}O_{36}(RSi)_2O]^{4-}$ and $[\gamma\text{-}SiW_{10}O_{36}(RSiO)_4]^{4-}$: Synthesis and structural determination by Multinuclear NMR Spectroscopy and Matrix-Assisted Laser Desorption/Ionization Time-of-Flight Mass Spectrometry. *Chem. Eur. J.* **2000**, *6*, 105–110. [CrossRef]
29. Kim, G.-S.; Hagen, K.S.; Hill, C.L. Synthesis, structure, spectroscopic properties, and hydrolytic chemistry of organophosphonoyl polyoxotungstates of formula $[C_6H_5P(O)]_2X^{n+}W_{11}O_{39}]^{(8-n)-}$ (X = P^{5+}, Si^{4+})]. *Inorg. Chem.* **1992**, *31*, 5316–5324. [CrossRef]
30. Mayer, C.R.; Thouvenot, R. Organophosphoryl derivatives of trivacant tungstophosphates of general formula α-A-$[PW_9O_{34}(RPO)_2]^{5-}$: Synthesis and structure determination by Multinuclear Magnetic Resonance Spectroscopy.(^{31}P, ^{183}W). *Dalton Trans.* **1998**, 7–13. [CrossRef]
31. Mayer, C.R.; Herson, P.; Thouvenot, R. Organic–inorganic hybrids based on polyoxometalates. Synthesis and structural characterization of bis(organophosphoryl) decatungstosilicates $[\gamma\text{-}SiW_{10}O_{36}(RPO)_2]^{4-}$. *Inorg. Chem.* **1999**, *38*, 6152–6158. [CrossRef] [PubMed]

32. Sun, Z.-G.; Liu, Q.; Liu, J.-F. Synthesis and spectroscopic characterization of organophosphoryl polyoxotungstates $[C_6H_{11}P(O)]_2X^{n+}W_{11}O_{39}{}^{(8-n)-}$ (X^{n+} = P^{5+}, Si^{4+}, B^{3+}, Ga^{3+}). *Polyhedron* **2000**, *19*, 125–128. [CrossRef]
33. Boujtita, M.; Boixel, J.; Blart, E.; Mayer, C.R.; Odobel, F. Redox properties of hybrid Dawson type polyoxometalates disubstituted with organo-silyl or organo-phosphoryl moieties. *Polyhedron* **2008**, *27*, 688–692. [CrossRef]
34. Sun, Z.-G.; Zhu, Z.-M.; You, W.-S. Synthesis and characterization of organophosphoryl polyoxotungstates $[RP(O)]_2X^{n+}W_{11}O_{39}]^{(8-n)-}$ (X^{n+} = P^{5+}, Si^{4+}, Ge^{4+}, Ga^{3+}). *Transition Met. Chem.* **2003**, *28*, 849–851. [CrossRef]
35. Schroden, R.C.; Blanford, C.F.; Melde, B.J.; Johnson, B.J.S.; Stein, A. Direct synthesis of ordered macroporous silica materials functionalized with polyoxometalate clusters. *Chem. Mater.* **2001**, *13*, 1074–1081. [CrossRef]
36. Mayer, C.R.; Cabuil, V.; Lalot, T.; Thouvenot, R. Incorporation of magnetic nanoparticles in new hybrid networks based on heteropolyanions and polyacrylamide. *Angew. Chem. Int. Ed.* **1999**, *38*, 3672–3675. [CrossRef]
37. Mayer, C.R.; Neveu, S.; Cabuil, V. A Nanoscale hybrid system based on gold nanoparticles and heteropolyanions. *Angew. Chem. Int. Ed.* **2002**, *41*, 501–503. [CrossRef]
38. Cannizzo, C.; Mayer, C.R.; Sécheresse, F.; Larpent, C. Covalent hybrid materials based on nanolatex particles and Dawson polyoxometalates. *Adv. Mater.* **2005**, *17*, 2888–2892. [CrossRef]
39. Villanneau, R.; Marzouk, A.; Wang, Y.; Ben Djamaa, A.; Laugel, G.; Proust, A.; Launay, F. Covalent grafting of organic–inorganic polyoxometalates hybrids onto mesoporous SBA-15: A key step for new anchored homogeneous catalysts. *Inorg. Chem.* **2013**, *52*, 2958–2965. [CrossRef] [PubMed]
40. Joo, N.; Renaudineau, S.; Delapierre, G.; Bidan, G.; Chamoreau, L.-S.; Thouvenot, R.; Gouzerh, P.; Proust, A. Organosilyl/-germyl polyoxotungstate hybrids for covalent grafting onto silicon surfaces: Towards molecular memories. *Chem. Eur. J.* **2010**, *16*, 5043–5051. [CrossRef] [PubMed]
41. Mercier, D.; Boujday, S.; Annabi, C.; Villanneau, R.; Pradier, C.-M.; Proust, A. Bifunctional polyoxometalates for planar gold surface nanostructuration and protein immobilization. *J. Phys. Chem. C* **2012**, *116*, 13217–13224. [CrossRef]
42. Duffort, V.; Thouvenot, R.; Afonso, C.; Izzet, G.; Proust, A. Straightforward synthesis of new polyoxometalate-based hybrids exemplified by the covalent bonding of a polypyridyl ligand. *Chem. Commun.* **2009**, 6062–6064. [CrossRef] [PubMed]
43. Elliott, K.J.; Harriman, A.; le Pleux, L.; Pellegrin, Y.; Blart, E.; Mayer, C.R.; Odobel, F.A. Porphyrin–polyoxometallate bio-inspired mimic for artificial photosynthesis. *Phys. Chem. Chem. Phys.* **2009**, *11*, 8767–8773. [CrossRef] [PubMed]
44. Matt, B.; Renaudineau, S.; Chamoreau, L.-M.; Afonso, C.; Izzet, G.; Proust, A. Hybrid polyoxometalates: Keggin and Dawson silyl derivatives as versatile platforms. *J. Org. Chem.* **2011**, *76*, 3107–3111. [CrossRef] [PubMed]
45. Odobel, F.; Severac, M.; Pellegrin, Y.; Blart, E.; Fosse, C.; Cannizzo, C.; Mayer, C.R.; Eliott, K.J.; Harriman, A. Coupled sensitizer–catalyst dyads: Electron-transfer reactions in a perylene–polyoxometalate conjugate. *Chem. Eur. J.* **2009**, *15*, 3130–3138. [CrossRef] [PubMed]
46. Liu, L.; Hu, L.; Liu, Q.; Du, Z.-L.; Li, F.-B.; Li, G.-H.; Zhu, X.-J.; Wong, W.-Y.; Wang, L.; Li, H. Synthesis and photoelectric properties of new Dawson-type polyoxometalate-based dimeric and oligomeric Pt(II)-acetylide inorganic–organic hybrids. *Dalton Trans.* **2015**, *44*, 306–315. [CrossRef] [PubMed]
47. Villanneau, R.; Ben Djamâa, A.; Chamoreau, L.-M.; Gontard, G.; Proust, A. Bisorganophosphonyl and -organoarsenyl derivatives of heteropolytungstates as hard ligands for early-transition-metal and lanthanide cations. *Eur. J. Inorg. Chem.* **2013**, 1815–1820. [CrossRef]
48. Villanneau, R.; Racimor, D.; Messner-Henning, E.; Rousselière, H.; Picart, S.; Thouvenot, R.; Proust, A. Insights into the coordination chemistry of phosphonate derivatives of heteropolyoxotungstates. *Inorg. Chem.* **2011**, *50*, 1164–1166. [CrossRef] [PubMed]
49. Carraro, M.; Sandei, L.; Sartorel, A.; Scorrano, G.; Bonchio, M. Hybrid polyoxotungstates as second-generation POM-based catalysts for microwave-assisted H_2O_2 activation. *Org. Lett.* **2006**, *8*, 3671–3674. [CrossRef] [PubMed]
50. Guillemot, G.; Matricardi, E.; Chamoreau, L.-M.; Thouvenot, R.; Proust, A. Oxidovanadium(V) anchored to silanol-functionalized polyoxotungstates: Molecular models for single-site silica-supported vanadium catalysts. *ACS Catal.* **2015**, *5*, 7415–7423. [CrossRef]

51. Tézé, A.; Michelon, M.; Hervé, G. Syntheses and structures of the tungstoborate anions. *Inorg. Chem.* **1997**, *36*, 505–509. [CrossRef]
52. Nsouli, N.H.; Chubarova, E.V.; Al-Oweini, R.; Bassil, B.S.; Sadakane, M.; Kortz, U. Organoruthenium-containing heteropoly-23-tungstate family $[\{Ru(L)\}_2(\alpha\text{-}XW_{11}O_{39})_2WO_2]^{m-}$ (L = benzene, *p*-cymene; X = Ge^{IV}, Si^{IV}, *m* = 10; B^{III}, *m* = 12). *Eur. J. Inorg. Chem.* **2013**, 1742–1747. [CrossRef]
53. Reinoso, S.; Dickman, M.H.; Matei, M.F.; Kortz, U. 13-Tungstoborate stabilized by an organostannoxane hexamer. *Inorg. Chem.* **2007**, *46*, 4383–4385. [CrossRef] [PubMed]
54. Reinoso, S.; Vitoria, P.; San Felices, L.; Gutiérrez-Zorrilla, J.M. Diiron(III)-containing 23-tungsto-2-borate: First evidence of 3d metal substitution in the $\{BW_{13}\}$ framework. *Eur. J. Inorg. Chem.* **2013**, 1644–1648. [CrossRef]
55. Brown, I.D.; Alternatt, D. Bond-valence parameters obtained from a systematic analysis of the inorganic crystal structure database. *Acta Crystallogr.* **1985**, *B41*, 244–247. [CrossRef]
56. Dougherty, D.A. The cation-π interaction. *Acc. Chem. Res.* **2013**, *46*, 885–893. [CrossRef] [PubMed]
57. Nishio, M.; Umezawa, Y.; Fantini, J.; Weiss, M.S.; Chakrabarti, P. CH−π hydrogen bonds in biological macromolecules. *Phys. Chem. Chem. Phys.* **2014**, *16*, 12648–12683. [CrossRef] [PubMed]
58. Gallivan, J.P.; Dougherty, D.A. A computational study of cation–π interactions *vs.* salt bridges in aqueous media: Implications for protein engineering. *J. Am. Chem. Soc.* **2000**, *122*, 870–874. [CrossRef]
59. Goto, Y.; Kamata, K.; Yamaguchi, K.; Uehara, K.; Hikichi, S.; Mizuno, N. Synthesis, structural characterization, and catalytic performance of dititanium-substituted γ-Keggin silicotungstate. *Inorg. Chem.* **2006**, *45*, 2347–2356. [CrossRef] [PubMed]
60. Maeda, H.; Maeda, T.; Mizuno, K. Absorption and fluorescence spectroscopic properties of 1- and 1,4-silyl-substituted naphthalene derivatives. *Molecules* **2012**, *17*, 5108–5125. [CrossRef] [PubMed]
61. Xie, Y.; Zhang, Q.; Zhao, Z.; Wu, X.; Chen, S.; Lu, C. New optical supramolecular compound constructed from a polyoxometalate cluster and an organic substrate. *Inorg. Chem.* **2008**, *47*, 8086–8090. [CrossRef] [PubMed]
62. Matt, B.; Coudret, C.; Viala, C.; Jouvenot, D.; Loiseau, F.; Izzet, G.; Proust, A. Elaboration of covalently linked polyoxometalates with ruthenium and pyrene chromophores and characterization of their photophysical properties. *Inorg. Chem.* **2011**, *50*, 7761–7768. [CrossRef] [PubMed]
63. Sun, Z.-G.; You, W.-S.; Li, J.; Liu, J.-F. Synthesis and spectroscopic characterization of organophosphoryl polyoxotungstates α-$[\{RP(O)\}_2SiW_{11}O_{39}]^{4-}$. *Inorg. Chem. Commun.* **2003**, *6*, 238–240. [CrossRef]
64. Pretsch, E.; Clerc, T.; Seibl, J.; Simon, W. *Tables of Spectral Data for Structure Determination of Organic Compounds*; Springer-Verlag: Berlin, Germany, 1989.
65. Hervé, G.; Tézé, A. Study of α and β-enneatungstosilicates and germanates. *Inorg. Chem.* **1977**, *16*, 2115–2117. [CrossRef]
66. Fulmer, G.R.; Miller, A.J. M.; Sherden, N.H.; Gottlieb, H.E.; Nudelman, A.; Stoltz, B.M.; Bercaw, J.E.; Goldberg, K.I. NMR chemical shifts of trace impurities: Common laboratory solvents, organics, and gases in deuterated solvents relevant to the organometallic chemist. *Organometallics* **2010**, *29*, 2176–2179. [CrossRef]
67. *CrysAlisPro Software System*; Version 171.36.24; Agilent Technologies UK Ltd.: Oxford, UK, 2012.
68. Dolomanov, O.V.; Bourhis, L.J.; Gildea, R.J.; Howard, J.A.K.; Puschmann, H. A complete structure solution, refinement and analysis program. *J. Appl. Crystallogr.* **2009**, *42*, 339–341. [CrossRef]
69. Sheldrick, G.M. A short history of SHELX. *Acta Crystallogr.* **2008**, *A64*, 112–122. [CrossRef] [PubMed]
70. Spek, A.L. Structure validation in chemical crystallography. *Acta Crystallogr.* **2009**, *D65*, 148–155. [CrossRef] [PubMed]
71. Farrugia, L.J. *WinGX* suite for small-molecule single-crystal crystallography. *J. Appl. Crystallogr.* **1999**, *32*, 837–836. [CrossRef]
72. Neese, F. The ORCA program system. *Wiley Interdiscip. Rev. Comput. Mol. Sci.* **2012**, 73–78. [CrossRef]
73. Becke, A.D. Density-functional exchange-energy approximation with correct asymptotic-behavior. *Phys. Rev. A* **1988**, *38*, 3098–3100. [CrossRef]
74. Perdew, J.P. Density-functional approximation for the correlation energy of the inhomogeneous electron gas. *Phys. Rev. B* **1986**, *33*, 8822–8824. [CrossRef]
75. Grimme, S.; Antony, J.; Ehrlich, S.; Krieg, H. A consistent and accurate *ab initio* parametrization of Density Functional Dispersion Correction (DFT-D) for the 94 elements H–Pu. *J. Chem. Phys.* **2010**, *132*, 154014. [CrossRef] [PubMed]

76. Grimme, S.; Ehrlich, S.; Goerigk, L. Effect of the damping function in dispersion corrected density functional theory. *J. Comput. Chem.* **2011**, *32*, 1456–1465. [CrossRef] [PubMed]
77. Weigend, F.; Ahlrichs, R. Balanced basis sets of split valence, triple zeta valence and quadruple zeta valence quality for H to Rn: Design an assessment of accuracy. *Phys. Chem. Chem. Phys.* **2005**, *7*, 3297–3305. [CrossRef] [PubMed]
78. Andrae, D.; Haeussermann, U.; Dolg, M.; Stoll, H.; Preuss, H. Energy-adjusted *ab initio* pseudopotentials for the second and third row transition elements. *Theor. Chim. Acta* **1990**, *77*, 123–141. [CrossRef]
79. Hirata, S.; Head-Gordon, M. Time-dependent density functional theory within the Tamm-Dancoff approximation. *Chem. Phys. Lett.* **1999**, *314*, 291–299. [CrossRef]
80. Becke, A.D. Density-functional thermochemistry. III. The role of exact exchange. *J. Chem. Phys.* **1993**, *98*, 5648–5652. [CrossRef]
81. Neese, F.; Wennmohs, F.; Hansen, A.; Becker, U. Efficient, approximate and parallel Hartree–Fock and hybrid DFT calculations. A 'Chain-Of-Spheres' algorithm for the Hartree–Fock exchange. *Chem. Phys.* **2009**, *356*, 98–109. [CrossRef]
82. Izsak, R.; Neese, F. An overlap fitted chain of spheres exchange method. *J. Chem. Phys.* **2011**, *135*, 144105. [CrossRef] [PubMed]
83. Petrenko, T.; Kossmann, S.; Neese, F. Efficient time-dependent density functional theory approximations for hybrid density functionals: Analytical gradients and parallelization. *J. Chem. Phys.* **2011**, *134*, 054116. [CrossRef] [PubMed]